Geoscience Frontiers 15 (2024) 101867

Contents lists available at ScienceDirect

Geoscience Frontiers

journal homepage: www.elsevier.com/locate/gsf

Research Paper

In situ apatite and carbonate Lu-Hf and molybdenite Re-Os geochronology for ore deposit research: Method validation and example application to Cu-Au mineralisation

Alexander Simpson [a,b,1], Stijn Glorie [a,b,*], Martin Hand [a,b], Sarah E. Gilbert [c], Carl Spandler [a], Marija Dmitrijeva [d], Greg Swain [d], Angus Nixon [a], Jacob Mulder [a], Carsten Münker [e]

[a] Department of Earth Sciences, University of Adelaide, SA 5005, Australia
[b] Mineral Exploration Cooperative Research Centre, University of Adelaide, SA 5005, Australia
[c] Adelaide Microscopy, University of Adelaide, SA 5005, Australia
[d] Fortescue, Level 2 87, Adelaide Terrace, East Perth, WA 6005, Australia
[e] Institute of Geology und Mineralogy, University of Köln, 50674 Köln, Germany

ARTICLE INFO

Article history:
Received 19 March 2024
Revised 9 May 2024
Accepted 13 May 2024
Available online 15 May 2024
Handling Editor: M. Santosh

Keywords:
Reaction-cell ICP-MS
In-situ geochronology
Lu-Hf
Re-Os
Iron Oxide Copper Gold
Metal fluids

ABSTRACT

The development of laser ablation inductively coupled plasma quadrupole tandem mass spectrometry (LA-ICP-Q-MS/MS) opens new opportunities to rapidly date a variety of hydrothermal minerals. Here we present *in situ* Lu-Hf and Re-Os dates for hydrothermal apatite and molybdenite, respectively. We further report the first *in situ* Lu-Hf dates for bastnäsite, dolomite, and siderite, and assess their potential for constraining ore deposit geochronology. For method validation, we report isotope-dilution Lu-Hf dates for apatite reference material Bamble-1 (1102 ± 5 Ma) and calcite reference material ME-1 (1531 ± 7 Ma), enabling improved accuracy on matrix-matched calibration for LA-ICP-MS/MS Lu-Hf dating. The new methods are applied to the Vulcan Iron-Oxide Copper-Gold (IOCG) prospect in the Olympic Cu-Au Province of South Australia. Such deposits have been difficult to accurately date, given the general lack of reliable mineral geochronometers that are cogenetic with IOCG mineralisation. Hydrothermal apatite Lu-Hf dates and molybdenite Re-Os dates demonstrate that mineralisation at Vulcan largely occurred at ca. 1.6 Ga, contemporaneous with the world class Olympic Dam deposit. Our data also indicates that the Lu-Hf system in apatite is more robust than the U-Pb system for determining the timing of primary apatite formation in an IOCG system. We further demonstrate that dolomite can retain Lu-Hf growth ages over an extended time period (>1.5 billion years), providing constraints on the timing of primary ore mineral crystallisation during brecciation and IOCG mineralisation. Finally, late Neoproterozoic (ca. 589–544 Ma) and Carboniferous (ca. 334 ± 7 Ma) Lu-Hf dates were obtained for texturally late Cu-bearing carbonate veins, illustrating that the carbonate Lu-Hf method allows direct dating of Cu remobilisation events. This has important implications for mineral exploration as the remobilised Cu may have been transferred to younger deposits hosted in Neoproterozoic sedimentary basins overlaying the Olympic IOCG province.

1. Introduction

A robust geochronological framework is crucial to develop effective strategies for mineral exploration, particularly in ancient geological terranes with complex evolutionary histories. In this regard, dating of hydrothermal mineral assemblages within a deposit is often desired to directly determine the timing of ore formation. Given the wide variety of potential sources of mineralising fluids and mechanisms for metal precipitation (McCuaig et al., 2010), establishing synchronicity between mineral precipitation from a fluid and a given geological event (e.g. magmatism or fault movement) can be an important step in determining the genesis of mineral deposits. Although other lines of evidence (such as petrology and mineral or whole-rock chemistry and isotopic data) can be used to infer the origin of a mineral deposit, this can be

* Corresponding author at: Department of Earth Sciences, University of Adelaide, SA 5005, Australia.
E-mail address: stijn.glorie@adelaide.edu.au (S. Glorie).
[1] British Geological Survey, Nottingham, UK.

https://doi.org/10.1016/j.gsf.2024.101867

complicated if multiple fluid-generating events have affected the region (e.g. multiple magmatic intrusions). Even when mineral deposit genesis is well constrained, this may not tell the full story. For instance, mineral deposits can undergo a variety of post-formation events that may affect their preservation potential, such as metamorphism and hydrothermal activity (Bastrakov et al., 2007; Duuring et al., 2010; Hall et al., 2018; Glorie et al., 2019a, b; Ehrig et al., 2021). Additionally, as the global demand for metals rises, the minerals industry is increasingly searching for economic mineralisation under cover (e.g. Reid, 2019) and within cover sequences (e.g. Leach et al., 2005). It can be challenging to fully understand deeply buried mineral deposits due to the lack of outcrop and reliance on drill core samples. Understanding the timing of potential remobilisation events might dictate if exploration efforts should be focussed on primary basement (hypogene) vs remobilised (supergene) equivalents.

Zircon is the most commonly dated mineral (Faure and Mensing, 2005), and is capable of providing robust age constraints on a variety of geological processes, including mineral deposits (e.g. Claoué-Long et al., 1990; Campbell et al., 2014; Zhai et al., 2022). However, zircon cannot always be relied upon when dating mineral deposits as it is not commonly observed in cogenetic context with ore minerals (e.g. no zircon was identified in any of the samples analysed in this study). This is likely due to the generally low solubility of zircon in most crustal fluid compositions, and hence limited hydrothermal transport of zirconium (Wilke et al., 2012). Consequently, other mineral geochronometers must be explored to place temporal constraints on the mineralisation history of ore deposits.

Uranium-Pb dating has been applied to a variety of other minerals that can form in hydrothermal systems, such as apatite and titanite (Chew et al., 2014; Spandler et al., 2016; Cherry et al., 2018; Glorie et al., 2019b), Fe-oxides (Ciobanu et al., 2013; Courtney-Davies et al., 2020), monazite (Cherry et al., 2018; Cave et al., 2022), xenotime (Rasmussen et al., 2007) and potentially carbonates (Roberts, 2020). There are, however, some complications. Firstly, although Fe-oxides can occasionally be dated (Ciobanu et al., 2013; Corriveau et al., 2016; Courtney-Davies et al., 2020; Skirrow, 2022), the most abundant mineral amenable to radiometric dating in IOCG deposits is often apatite (e.g. Cave et al., 2018). However, apatite has a relatively low closure temperature for Pb volume diffusion (~450 °C; Cherniak et al., 1991; Cochrane et al., 2014) and is susceptible to resetting during fluid interactions (e.g. Harlov et al., 2005; Glorie et al., 2019b). Although many IOCGs are thought to form at temperatures lower than ~450 °C (e.g. Corriveau et al., 2016; Skirrow, 2022), post-formational heating and/or fluid-induced dissolution-recrystallisation may disturb the isotopic U-Pb system. Secondly, many ore deposits contain high absolute concentrations of Pb and minerals such as apatite, titanite and carbonates can incorporate significant volumes of this non-radiogenic Pb cargo into their crystal structure during formation (Chew et al., 2014; Roberts and Walker, 2016). Consequently, Pb isotope ratios can be strongly dominated by common Pb, leading to large uncertainties in U-Pb age calculations, and potentially negating the utility of U-bearing minerals that have propensity to accommodate Pb. Lastly, traditionally dated minerals will not necessarily occur in every mineral assemblage within a deposit, and hence it is beneficial to have access to a wide range of datable minerals to best constrain mineralogically diverse domains.

The development of novel laser ablation geochronological techniques using reaction-cell mass-spectrometry (LA-ICP-MS/MS) (e.g. Hogmalm et al., 2019; Simpson et al., 2021) has enabled direct *in situ* Lu-Hf and Re-Os dating of a variety of hydrothermal minerals such as apatite, fluorite, molybdenite and carbonates within cogenetic context of ore minerals (Gillespie et al., 2022; Simpson et al., 2022; Glorie et al., 2023, 2024b; Tamblyn et al., 2024). In contrast to traditional bulk-dissolution approaches (e.g. Scherer et al., 2001; Selby and Creaser, 2001; Barfod et al., 2003; Maas et al., 2022), the novel laser-ablation approach requires minimal sample preparation and has the potential to quickly and efficiently obtain direct, spatially resolved, age constraints for hydrothermal minerals. Consequently, multi-mineral LA-ICP-MS/MS geochronology provides a new avenue to complement U-Pb dating, and may be able to provide a more robust temporal framework for hydrothermal processes (e.g. Glorie et al., 2024b).

The Olympic Cu-Au Province in the Gawler Craton in Southern Australia (e.g. Reid, 2019) provides a natural laboratory to test the application of *in situ* Lu-Hf and Re-Os analysis to obtain a detailed geochronological framework for the timing of IOCG mineralisation and potential remobilisation. The Olympic Cu-Au Province hosts a variety of mineral deposits and prospects, including the world class Olympic Dam iron oxide copper gold (IOCG) deposit, as well as major deposits such as Carrapateena and Prominent Hill (Hand et al., 2007; Skirrow et al., 2007; Reid, 2019). The timing of IOCG mineralisation in the Olympic Cu-Au Province has been extensively studied and is broadly synchronous with the intrusion of the ~1.59 Ga Hiltaba Suite and its extrusive equivalent, the Gawler Range Volcanics (GRV) (Johnson and Cross, 1995; Skirrow et al., 1999; Skirrow et al., 2007; Reid, 2019). However, recent studies at Olympic Dam have indicated the presence of multiple events that have modified the deposit to varying extents, spanning from original deposit formation at ca. 1.6 Ga to the ca. 0.5 Ga Delamerian Orogeny (e.g. Ehrig et al., 2021; Maas et al., 2022). Given this protracted record of deposit modification, a detailed geochronological framework is essential for understanding primary Cu ore formation and subsequent remobilization events to promote effective mineral exploration.

In this paper, we apply the *in situ* Lu-Hf method (Simpson et al., 2021) to apatite and carbonate minerals that are in textural equilibrium with primary Cu mineralisation in the Vulcan IOCG prospect. Vulcan is located ~30 km northeast from the Olympic Dam deposit within the Olympic Cu-Au Province (Fig. 1) and has been explored through multiple drilling campaigns.

The Lu-Hf system has been demonstrated to be more resistant to isotopic resetting in apatite and calcite compared to the U-Pb system, due to its higher closure temperature (e.g. Barfod et al., 2005; Gillespie et al., 2022; Maas et al., 2022; Simpson et al., 2022; Glorie et al., 2024b). Hafnium is relatively immobile in many hydrothermal fluids (Brugger et al., 2016), and is not readily incorporated into common hydrothermal minerals, such as apatite (Barfod et al., 2005; Glorie et al., 2022) and carbonates (e.g. calcite and siderite; Maas et al., 2022; Simpson et al., 2022). We assess the advantages and limitations of Lu-Hf compared to U-Pb dating in hydrothermal apatite and validate the laser-ablation Lu-Hf chronometer in apatite and calcite against the conventional isotope-dilution method. We further explore the potential for laser ablation Lu-Hf dating to constrain the timing of other hydrothermal carbonate minerals that are commonly found in IOCG deposits (dolomite, siderite, and bastnäsite). In addition, we test the *in situ* Re-Os method (Hogmalm et al., 2019), which was recently refined by Tamblyn et al. (2024), to constrain the timing of hydrothermal molybdenite formation in the Vulcan prospect.

2. Geological setting

The Vulcan IOCG prospect covers nearly 12 km^2 (Fig. 2) and, like other IOCG deposits in this region, is covered by Neoproterozoic to recent sedimentary units. Copper mineralisation is hosted within hematite-dominated brecciated and hematite-altered rocks, with textures and paragenetic evolution similar to other IOCG prospects and deposits in the region (Reeves et al., 1990; Reid et al., 2013).

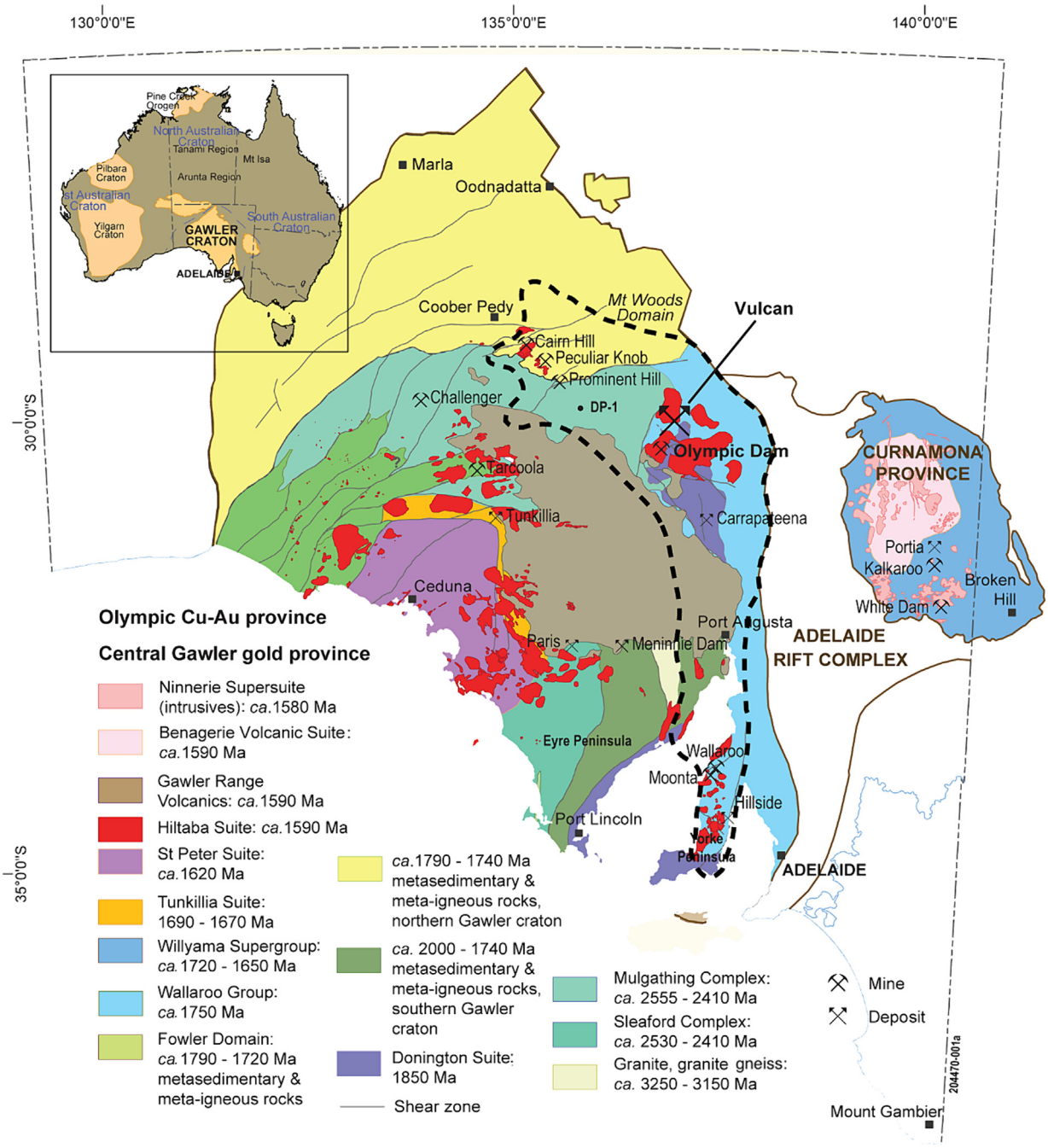

Fig. 1. Simplified geological map of the Gawler Craton, showing the location of mineral deposits and prospects (including Vulcan). The inset shows the position of the Gawler Craton in relation to the rest of Australia and Australia's major crustal blocks (after Reid, 2019). The dashed line shows the outline of the Olympic Cu-Au Province.

Gravity and magnetic data suggest the alteration system is potentially similar in size to Olympic Dam, but under a significantly thicker (ca. 900 m) blanket of sedimentary cover (compared to ca. 350 m at Olympic Dam). The rocks at Vulcan are heavily brecciated and extensively altered, making identification of the original host rocks difficult. Regionally, the basement consists of the ca. 1850 Ma Donington Suite granite, a metasedimentary succession deposited at ca. 1750 Ma (Wallaroo Group), and younger Hiltaba Suite granites that intruded at ca. 1590 Ma (Reid et al., 2013; Reid, 2019). The Vulcan prospect is hosted by the siliciclastic Wallaroo Group metasediments, quartzofeldspathic granite (U-Pb zircon 1743 ± 7 Ma; Reid et al., 2013; Reid, 2019), granitic gneiss, pegmatite, and undeformed to highly deformed mafics of unknown age. Conventional (solution-based) Re-Os dating of molybdenite that formed in association with hematite breccias at Vulcan yielded an age of 1586 ± 8 Ma (Reid et al., 2013). Hence, alteration and mineralisation appear at least partly contemporaneous with the main ore stage at Olympic Dam (e.g. Johnson and Cross, 1995; McPhie et al., 2011; Ciobanu et al., 2013; Cherry et al., 2018).

Olympic Dam has undergone a complex evolution since formation, responding to many regional tectonic events, such as the Musgrave Albany-Fraser Orogney associated with Rodinia construction at ca. 1200–1100 Ma, the ca. 800 Ma break-up of Rodinia, and the ca. 515–490 Ma Delamerian Orogeny (e.g. Huang et al., 2015; Cherry et al., 2018; Ehrig et al., 2021; Maas et al., 2022). For instance, based on U-Pb dating of uraninite, Pb isotopes in sul-

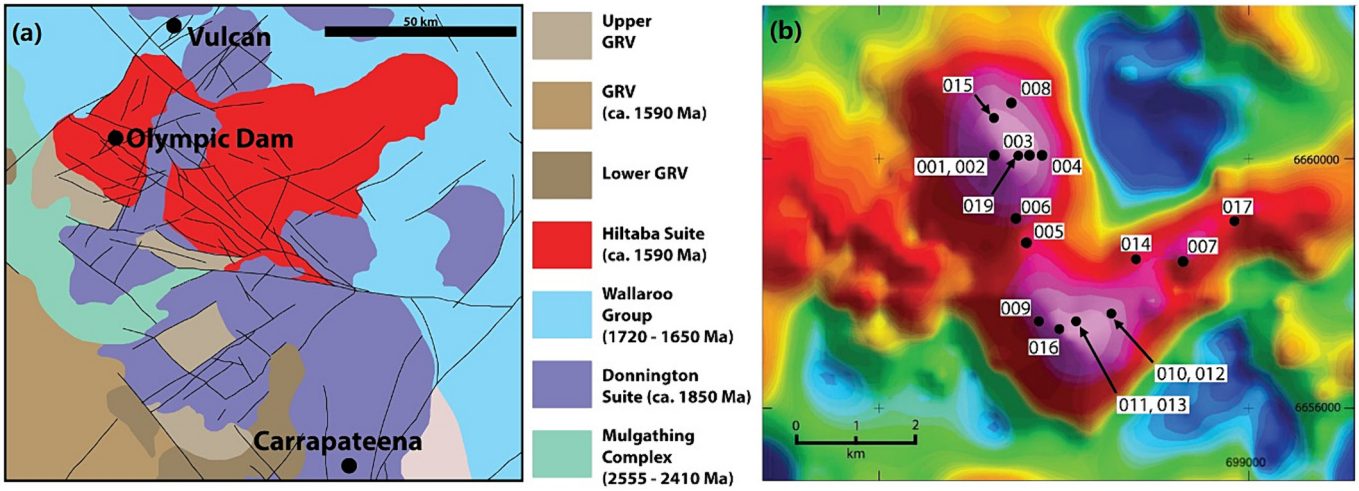

Fig. 2. L(a) Geological map showing the location of the Vulcan IOCG prospect relative to Olympic Dam and Carrapateena. (b)Pseudo-colour residual gravity image of the Vulcan IOCG prospect showing the location of drill holes (from Reid et al., 2013). Drill hole names are abbreviated from full names (i.e. VUD0019 becomes 019).

phides, and bulk U/Pb ratios, Ehrig et al. (2021) argued that a significant 'upgrading' event occurred at ca. 700–500 Ma, up to a billion years after initial mineralisation at Olympic Dam. This event likely involved an influx of U, but may also have been associated with an increase in metals such as Cu.

Although monazite and xenotime U-Pb dates of ca. 1450–1400 Ma have been recorded for the Acropolis and Oak Dam East prospects within the Olympic Cu-Au Province (Davidson et al., 2007; Cherry et al., 2018), a systematic geochronological framework that includes potentially younger mineral assemblages in the Olympic Province is currently lacking in publicly accessible literature. Glorie et al. (2023) recently dated ca. 502 Ma Cu remobilisation in fluorite-calcite veins within Stuart Shelf sedimentary cover sequences over the Olympic Cu-Au Province, which is broadly contemporaneous with the upgrading event identified at Olympic Dam (Ehrig et al., 2021). However, the significance of the spectrum of radiometric dates obtained in the Olympic Cu-Au Province for metal endowment and redistribution is yet to be fully appreciated. Given the limited previous geochronological work at the Vulcan prospect, it remains unclear if the alteration and mineralisation history occurred in a single stage at ca. 1590 Ma as recorded by conventional molybdenite Re-Os dating (Reid et al., 2013), or is a complex multi-stage system similar to that recorded at Olympic Dam.

3. Samples and petrographic descriptions

Hematite breccias at Vulcan consist of fine grained 'milled' breccias, as well as massive 'steely' hematite breccias. Both breccia types have similar mineralogy; hematite with minor to abundant magnetite, pyrite, carbonate minerals (mostly dolomite, siderite and ankerite), as well as minor apatite, chalcopyrite, quartz and chlorite. In rare cases, molybdenite and/or bastnäsite are present in the matrix. Minor late veins cut across both fine-grained breccias and massive steely hematite. These veins are mostly carbonate and occasionally quartz-dominated, and commonly have visible chalcopyrite crystals present within them.

Samples were collected from three drill cores from the Vulcan prospect (Fig. 2). The majority of samples are from drill core VUD0019 (drilled in 2021), however a sample from VUD007 (the highest Cu grade drill core) and VUD0017 were also collected in order to determine whether the geochronological framework is reproducible across the deposit. VUD0019 was chosen because it intersected a significant (ca. 350 m) interval of iron-oxide alteration, ranging from veins and breccias to massive hematite, and towards the end of the drillhole hematite-magnetite. The interval is characterised by abundant coarse-grained apatite (up to ~5–7 mm), bastnäsite and molybdenite, and coarse-grained dolomite-chalcopyrite veins cross-cutting the primary alteration assemblage. The sample naming scheme refers to the drill core number and the sample interval in meters (e.g. 019-1263 corresponds to a sample from the 1263-m interval of drill hole VUD0019).

4. Analytical methods

4.1. Scanning electron microscope

The samples were prepared as 2.5 cm epoxy disks and imaged using a Hitachi SU38000 scanning electron microscope (SEM). Both backscattered electron (BSE) imaging and mineral liberation analysis (MLA) were performed. Maps were acquired with the SEM operating at 20 kV and a magnification of 90 × .

4.2. LA-ICP-MS/MS analysis

All LA-ICP-MS/MS analyses were conducted at Adelaide Microscopy (The University of Adelaide) using a RESOlution-LR 193 nm excimer laser ablation system (Applied Spectra), with a S155 sample chamber (Laurin Technic), coupled to an Agilent 8900x ICP-MS/MS. N_2 gas was added after the sample chamber, but before the plasma, to improve sensitivity (Hu, 2008). In all cases, the ICP was first tuned without reaction gas in the collision cell, to establish a robust and consistent plasma (Th/ThO < 0.2%, Th/U of 1.00–1.05). Following this, tuning was conducted in reaction gas mode for each application. Settings were then optimised and adjusted to minimise isobaric interferences on target masses, and to promote sensitivity on low abundance isotopes (Simpson et al., 2021). Laser parameters, lens voltages, and ICP-MS/MS plasma conditions for all methods are detailed in Supplementary Data Text S1.

4.2.1. In situ U-Pb dating

LA-ICP-MS/MS U-Pb dating was conducted following the method outlined in Gilbert and Glorie (2020), which uses NH_3 gas to remove ^{204}Hg, allowing for interference-free measurement

of ^{204}Pb. A laser beam diameter of 43 μm was used with a fluence of ca. 3.5 J/cm^2 and repetition rate of 5 Hz. All Pb isotopes were measured 'on mass' and U was measured as UNH^+ (a mass shift of + 15 amu; Gilbert and Glorie, 2020). A sample-standard bracketing approach was used to correct for drift as well as laser induced and ICP induced fractionation, with MAD apatite (Thomson et al., 2012; Chew et al., 2014) and NIST-610 glass used as primary standards to calibrated the U/Pb and Pb/Pb ratios, respectively (cfr. Glorie et al., 2019b). ^{202}Hg was monitored to demonstrate interference-free ^{204}Pb measurements. Apatite 401 (Thompson et al., 2016) was used as secondary reference material for accuracy verification (Supplementary Data Fig. S1). All data processing (e.g. background subtractions, drift corrections, ratio normalisations, and trace element abundance calculations) was conducted using the LADR software (Norris and Danyushevsky, 2018). Age calculation and isochron plotting was conducted in IsoplotR (Vermeesch, 2018).

4.2.2. In situ Lu-Hf dating

Lu-Hf dating was conducted in 4 analytical sessions, following protocols in Simpson et al. (2021) and Simpson et al. (2022). For apatite and bastnäsite, laser diameters of 43–120 μm were used, with a repetition rate of 10 Hz and fluence of ca. 3.5 J/cm^2. For dolomite and siderite, a laser diameter of 257 μm was used, with a repetition rate of 10 Hz and a fluence of ca. 10 J/cm^2. The Lu-Hf method relies on reacting Hf with NH_3 gas, with the reaction of isobaric Lu and Yb isotopes being negligible. Hf reacts to form multiple reaction products, with gas flows tuned to promote formation of $Hf(NH)(NH_2)(NH_3)_3$ (+82 amu). Both Lu and Yb preferentially react with one more H than Hf, with $Lu(NH)(NH_2)(NH_3)_3^+$ forming at a rate of 0.003% (relative to Lu measured on mass) and $Yb(NH)(NH_2)(NH_3)_3^+$ forming at a rate of ~0.00003% (relative to Yb measured on mass) (Simpson et al., 2021). $Yb(NH)(NH_2)(NH_3)_3^+$ was not monitored, as the production is not high enough to affect the calculated ratios and is usually below detection limits. ^{175}Lu was measured as a proxy for ^{176}Lu, and ^{178}Hf was measured as a proxy for ^{177}Hf, assuming natural abundances. Additionally, a small correction (less than 1% for all samples) was applied to account for the interference of $Lu(NH)(NH_2)(NH_3)_3^+$ on $Hf(NH)(NH_2)(NH_3)_3^+$. Although we note that this correction was not significant for any sample analysed in this study, it was applied to all samples for consistency. Analyses included 30 s of background collection followed by 40 s of ablation. The following isotopes were measured, with dwell times in milliseconds in parentheses: ^{27}Al(2), ^{43}Ca(2), ^{47}Ti(2), ^{57}Fe(2), ^{88}Sr(2), $^{89+83}$Y(2), $^{90+83}$Zr(2), $^{140+15}$Ce(2), ^{146}Nd(2), ^{147}Sm(2), ^{172}Yb(5), ^{175}Lu(10), $^{175+82}$Lu(100), $^{176+82}$Hf(200), $^{178+82}$Hf(150). For detailed descriptions of the method, the reader is referred to Simpson et al. (2021 and 2022).

Data reduction was conducted in LADR (Norris and Danyushevsky, 2018) with a sample-standard bracketing approach used to calculate isotope ratios. The isotope ratios were first normalised to NIST-610, and subsequently corrected for laser-induced, matrix-dependant elemental fractionation using a matrix-matched reference material (MCRM). This correction is similar to that used in calcite U-Pb (Roberts et al., 2017) and mica Rb-Sr (Glorie et al., 2024a) geochronology, and relies on applying a correction factor derived from the percentage offset between the reference and measured isochron age. For the apatite Lu-Hf analyses, OD306 apatite (U-Pb, 1597 ± 7.1 Ma; Thompson et al., 2016) was used as MCRM and Bamble-1 apatite and HR-1 apatite were used as secondary reference materials to demonstrate accuracy. Although the Lu-Hf age of both reference materials is well constrained by long-term reproducible LA-ICP-MS/MS dates (Bamble-1 = 1098 ± 5 Ma and HR-1 = 344 ± 2 Ma; Glorie et al., 2024b), independent conventional Lu-Hf age constraints are desirable for accuracy verification. For the carbonate samples, MKED-1 calcite was used as MCRM and ME-1 calcite as secondary reference material. For MKED-1, the reference age is derived from cogenetic titanite (TIMS U-Pb, 1517.3 ± 0.32 Ma; Spandler et al., 2016; Simpson et al., 2022). The age of the ME-1 reference calcite is assumed to be the same as a titanite U-Pb age of 1530 ± 11 Ma from the same deposit (Duncan et al., 2011; Simpson et al., 2022). However, similar to the apatite reference materials, isotope-dilution Lu-Hf dates were not available at the time of LA-ICP-MS/MS method development. In this work, we present isotope-dilution inductively-coupled-plasma multi-collector mass-spectrometry (ID-ICP-MCMS) Lu-Hf dates for both Bamble-1 apatite and ME-1 calcite (see section 4.3). Calculated LA-ICP-MS/MS dates for all reference materials can be found in Supplementary Data Fig. S1. Inverse isochron dates and/or weighted means dates (where initial Hf is negligible; Simpson et al., 2022; Glorie et al., 2024b) were calculated in IsoplotR (Vermeesch, 2018) using the ^{176}Lu decay constant of 1.867 × 10^{-11} Myr^{-1} (Scherer et al., 2001; Söderlund et al., 2004). In some samples where the initial ^{177}Hf/^{176}Hf ratios of all analyses were low, the isochron was anchored to the default initial ^{176}Hf/^{177}Hf ratio of 0.28 29 ± 0.003 in IsoplotR (Vermeesch, 2024). All isochrons were calculated as a maximum likelihood function (including overdispersion where relevant) and the reported uncertainties include propagated external uncertainties on the decay constant and the calibration reference material (MCRM).

4.2.3. In situ Re-Os dating

In situ Re-Os isotope analysis followed the method described in Tamblyn et al. (2024). A laser fluence of ca. 3.5 J/cm^2 and a repetition rate of 5 Hz were used and the laser beam diameter was set at 43 μm or 67 μm (and 100 μm for the Q-Molyhill reference material) to achieve high sensitivity while keeping the detector in pulse detection mode. The *in situ* Re-Os method uses a gas mixture of CH_4 in He in the reaction cell, optimised to promote $^{187+14}OsCH_2^+$ reaction, while suppressing interference of $^{187+14}ReCH_2^+$ (Hogmalm et al., 2019; Tamblyn et al., 2024). However, an interference correction is required as ~1.16% of the ^{187}Re reacts with CH_4 in our analytical setup. The interference correction subtracts the proportion of reacted Re on mass 201 amu, based on the measured $^{185+14}$Re cps for each analysis and assuming the natural ^{185}Re/^{187}Re isotopic abundance (1.674), corrected for mass bias based on the measured ^{185}Re/^{187}Re ratio in NIST-610 (0.867% in this session). ^{185}Re was measured as a proxy for ^{187}Re assuming natural isotopic abundances. Analyses included 30 s of background collection followed by 40 s of ablation. The following isotopes were measured, with dwell times in milliseconds in parentheses: ^{34}S(2), ^{95}Mo(2), ^{185}Re(20), $^{185+14}$Re(50), $^{187+14}$Os(150), $^{189+14}$Os(150). For detailed descriptions of the method, the reader is referred to Hogmalm et al. (2019) and Tamblyn et al. (2024).

Data reduction was conducted in the LADR software (Norris and Danyushevsky, 2018) using Q-Molyhill molybdenite as the primary reference material for the Re/Os ratio calculations with an ID-TIMS ^{187}Os /^{187}Re ratio of 0.044699 ± 0.000166, corresponding to a weighted mean Re-Os date of 2624 ± 5 Ma (Tamblyn et al., 2024). The ^{189}Os/^{187}Os ratios were calibrated to synthetic sulphide standard NiS-3 (Gilbert et al., 2013), assuming natural isotopic abundances. Secondary reference molybdenites MDQ0252 and MDQ0221 from the Merlin deposit were used for accuracy verification with ID-TIMS Re-Os dates of 1520 ± 3 Ma and 1523 ± 6 Ma, respectively (Babo et al., 2017; Tamblyn et al., 2024). All Re-Os dates were calculated in IsoplotR (Vermeesch, 2018) using the ^{187}Re decay constant of 1.6668 ± 0.0034 × 10^{-11} Myr^{-1} (Kośler et al. 2003).

4.3. Isotope dilution Lu-Hf geochronology for apatite and carbonate reference materials

Lutetium-Hf isotope analysis for the Bamble-1 apatite and ME-1 calcite reference materials was conducted at the University of Cologne, Germany. Given the challenging low Hf concentrations (≤10 ppb) and extremely high Lu/Hf ratios (>400) in these materials, a modified analytical method from that described in Münker et al. (2001), Sprung et al. (2010) and Maas et al. (2022) was applied. The powdered samples (up to 2 g) were dissolved in 6 M HCl at room temperature (carbonates) and 120 °C (apatites and carbonates after initial dissolution), respectively. A ^{176}Lu-^{180}Hf mixed spike optimized for materials with high Lu/Hf ratios was added prior to sample digestion (same spike as used for the original decay constant determination in Scherer et al., 2001). The spiked samples underwent 24 hr of sample:spike equilibration, promoted by heating and sonication. Prior to column chemistry, the sample solutions were dried down and taken up in 3 M HCl. The solutions (ca. 10 mL total) were loaded in 3 N HCl onto Eichrom Ln Spec column 1 of Münker et al. (2001) and Bast et al. (2015), where Lutetium (in 6 N HCl) and, after 4 reservoirs of rinsing in 6 N HCl and 1 reservoir in 1 N HNO_3-1% H_2O_2, an impure Hf cut (in 2 N HF) was collected from this step. Subsequently, the Hf cut in 2 N HF was directly loaded on HFSE column 2 (BIORAD AG-1-X 8) of (Münker et al., 2001), followed by rinses in 4 mL 2 N HF, 10 mL 0.5 N HCl/0.5 N HF and elution of a virtually HREE-free Hf in 3 × 4 mL 6 N HNO_3-0.2 N HF. For some cases, Eichrom Ln Spec column step 1 was repeated for further clean-up of the Hf cut (Sprung et al., 2010). The procedural blanks measured in the sample runs were 13 pg and 78 pg for Lu while 9 pg and 15 pg for Hf (^{176}Hf/^{177}Hf assumed as 0.28216), respectively. This Hf blank was insignificant for apatite (0.4–0.9 mol%), but significant for carbonate (2.6–5 mol%).

Lutetium and Hf isotopes were measured on a Thermo-Finnigan Neptune MC-ICPMS equipped with a standard nickel sampler and H-type skimmer cones as well as two 10^{-12} Ohm Faraday detectors to record the ^{175}Lu and ^{177}Hf signals. Hafnium fractions were measured in 0.56 N HNO_3-0.2 N HF and aspirated via a PFA nebulizer and Cetac Aridus 2 desolvator (uptake rate 0.1 mL/min). Interferences from HREE were negligible due to the excellent separation of Hf from HREE in the 2-column procedure and due to the substantial enrichment of radiogenic ^{176}Hf in the samples. Mass bias and spike stripping corrections were done offline, using a ^{179}Hf/^{177}-Hf ratio of 0.7325 for internal normalization and all Hf isotope data are given relative to a value of 0.282160 for the Münster AMES standard that is isotopically indistinguishable from JMC-475 (Münker et al., 2001). Lutetium isotope dilution runs were done as described in Lagos et al. (2007). Resulting isochron dates were calculated in IsoplotR (Vermeesch, 2018), using the ^{176}Lu decay constant of 1.867 × 10^{-11} (Scherer et al., 2001; Söderlund et al., 2004). For the ME-1 sample, cogenetic diopside (dissolved in 6 mL HNO_3-HF) was included in the sample-set to provide an initial Hf isochron anchor. For Bamble-1, no other cogenetic mineral phases were available and a default IsoplotR anchor (^{176}Hf/^{177}Hf = 0.2829 ± 0.003) was used to calculate the isochron age (Vermeesch, 2024). However, given the highly radiogenic nature of the sample, the choice of anchor within the range of all plausible terrestrial bulk rock compositions makes no difference to the calculated date.

5. Results

5.1. Mineral liberation analysis

Fig. 3 displays the MLA maps for the analysed samples, including photos of the corresponding hand samples to give the MLA maps context. For coarse-grained dolomite samples 019-1263 and 019-1574, no MLA map was obtained, as mineralogy is visible to the naked eye. Consequently, only hand sample photos have been included for these samples.

Petrographic descriptions are listed in Table 1. In general, the drill core consists of highly altered brecciated quartz-feldspatic gneiss and interlayered mafic rocks. Common textures include massive hydrothermal Fe-oxide (both hematite and magnetite) forming in association with siderite and/or dolomite, pyrite, apatite, chlorite, sericite, molybdenite, quartz ± chalcopyrite (samples 019-1315, 019-1354, and 019-1414; Fig. 3). The breccias are clast-supported with variable but generally fine-grained matrix minerals. Fragments of hydrothermal Fe-oxide are included in the fine-grained breccia sample 017-1210, indicating that brecciation post-dates hydrothermal Fe-oxide formation. However, in many instances, fragments within breccia consist of older breccia, indicating more than one cycle of alteration and brecciation. Numerous late, cross-cutting veins occur, which appear to post-date brecciation and hydrothermal Fe-oxide formation. Of particular interest are chalcopyrite-bearing dolomite veins, which may record remobilisation of primary Cu mineralisation.

5.2. Geochronology

The radiometric dates are summarised in Table 2, and associated plots are displayed in Fig. 4 (ID-ICP-MCMS), Fig. 5 (apatite LA-ICP-MS/MS), Fig. 6 (carbonate LA-ICP-MS/MS) and Fig. 7 (molybdenite LA-ICP-MS/MS). All analytical data are included in Supplementary Data Table S1 (ID-ICP-MCMS) and Supplementary Data Table S2 (LA-ICP-MS/MS). All plots and dates were calculated in IsoplotR (Vermeesch, 2018). Age uncertainties are presented at 2SE level (expanded to account for data scatter if MSWD is great than expected for a single population; Vermeesch, 2018). Uncertainties for the MCRM used for matrix-offset calibration are propagated to all LA-ICP-MS/MS Lu-Hf dates. For all dating systems, decay constant uncertainties are propagated to the reported age uncertainties.

5.2.1. Isotope-dilution Lu-Hf geochronology results for secondary reference materials

The ID-ICP-MCMS Lu-Hf data for the secondary apatite and carbonate reference materials are presented as normal isochrons based on the ^{176}Lu/^{177}Hf and ^{176}Hf/^{177}Hf ratios and their 2σ uncertainties.

Bamble-1 apatite

Two apatite aliquots contained ca. 17 ppm Lu and ca. 0.01 ppm Hf, resulting in ^{176}Lu/^{177}Hf ratios of ca. 2400 and 2800. Given the highly radiogenic nature of the Hf (^{176}Hf/^{177}Hf = ca. 50 and 60), the choice of a realistic initial Hf anchor has little effect to the isochron age calculation. We used a ^{176}Hf/^{177}Hf anchor of 0.282 ± 0.001, encompassing nearly the entire range of terrestrial bulk rock ratios. The resulting Lu-Hf isochron date was calculated as 1102.1 ± 5.4 Ma (MSWD = 0.19). This is in excellent agreement to a previously published multi-session weighted mean LA-ICP-MS/MS Lu-Hf date of 1097.0 ± 5.3 Ma (Glorie et al., 2022, 2024b) and the LA-ICP-MS/MS results obtained in this study (1100 ± 14 Ma and 1104 ± 14 Ma).

ME-1 calcite

Two calcite aliquots contained ca. 4 ppm Lu and ca. 0.004 ppm Hf, corresponding to ^{176}Lu/^{177}Hf ratios of 2104 and 636, respectively. Similarly as for the apatite, the Hf is highly radiogenic (^{176}-Hf/^{177}Hf = ca. 18.7 and 61.3). Cogenetic diopside was used as an anchor for the isochron regression with a measured ^{176}Lu/^{177}Hf ratio of 0.2195 ± 0.0004 and a ^{176}Hf/^{177}Hf ratio of 0.288215 ± 0.000017. The resulting Lu-Hf isochron date was calculated as 1531.1 ± 7.4 Ma (MSWD = 0.04), which is in excellent agreement with

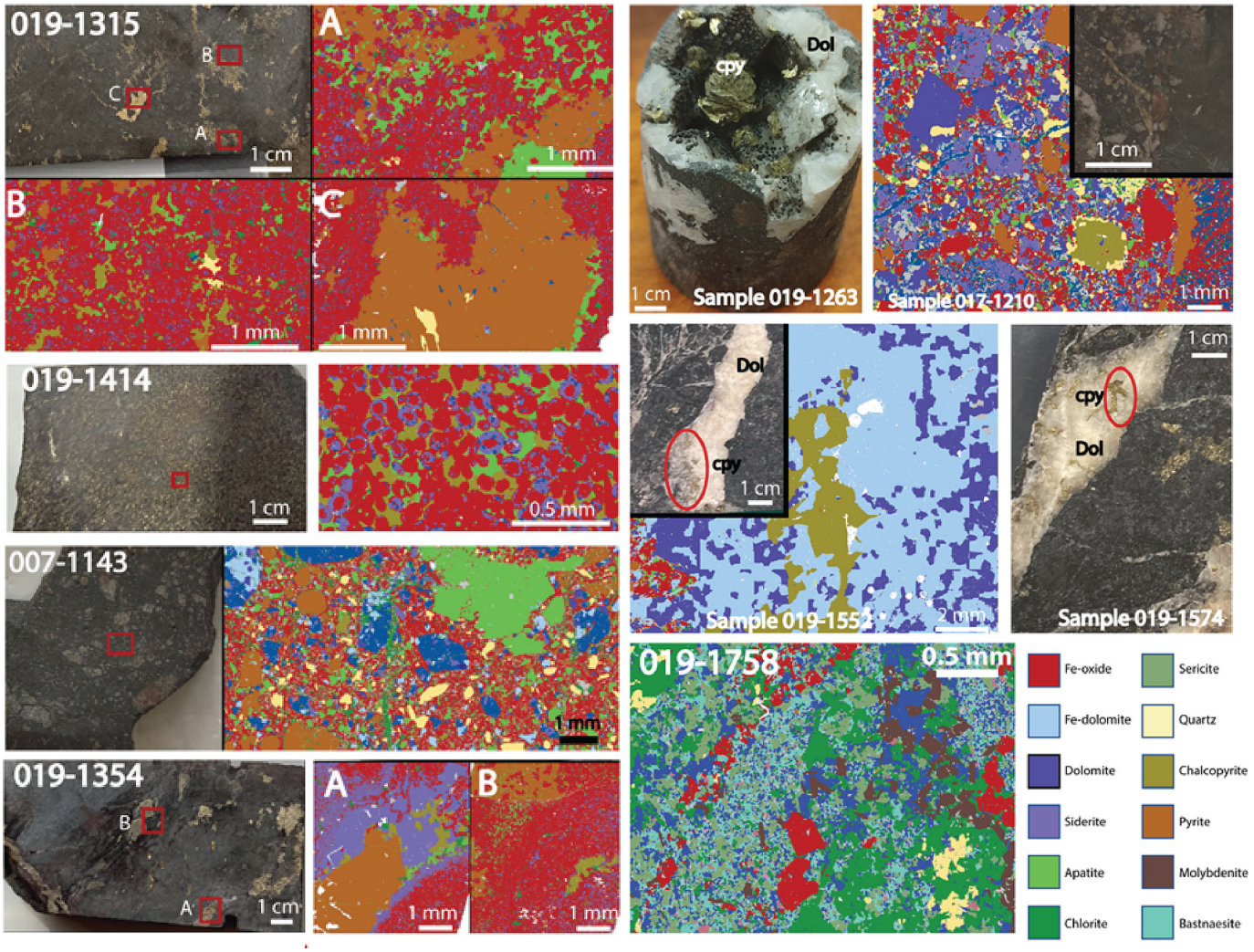

Fig. 3. Sample photographs and SEM mineral liberation analysis (MLA) mineral maps displaying the mineralogy and textures of the dated samples. Red boxes or circles on the drill core photos correspond to SEM MLA map locations. As samples 019-1263 and 019-1574 are coarse grained, they were not MLA mapped. (For interpretation of the references to colour in this figure legend, the reader is referred to the web version of this article.)

a cogenetic titanite U-Pb date of 1530 ± 11 Ma (Duncan et al., 2011) and with a previously published multi-session weighted mean LA-ICP-MS/MS Lu-Hf date of 1538 ± 9 Ma (Simpson et al., 2022).

5.2.2. In situ apatite u-pb and Lu-Hf geochronology results for Vulcan

The U-Pb geochronology data are presented on 3D isochrons in Tera-Wasserburg concordia plots based on the $^{238}U/^{206}Pb$, $^{207}Pb/^{206}Pb$, $^{204}Pb/^{206}Pb$ ratios, their 2σ uncertainties and uncertainty correlations. The isochrons are presented both as free regressions and anchored to Stacey and Kramers (1975) initial Pb ratios, where relevant. The measured U-Pb date (3D isochron, anchored to Stacey and Kramers, 1975) for secondary reference material 401 (526 ± 3.4 Ma) is in excellent agreement with the reference age of 525 ± 8 Ma (Thompson et al., 2016) (Table 2; Supplementary Data Fig. S1). The LA-ICP-MS/MS apatite Lu-Hf data are presented as inverse isochrons, based on the $^{176}Lu/^{176}Hf$ and $^{177}Hf/^{176}Hf$ ratios, their 2σ uncertainties and uncertainty correlations. All apatite Lu-Hf dates have been calibrated for laser induced matrix-dependant fractionation against the OD-306 apatite MCRM. The measured *in situ* Lu-Hf dates for secondary reference materials Bamble-1 (session 1: 1100 ± 14 Ma; session 2: 1104 ± 14 Ma) and HR-1 (session 1: 344 ± 4 Ma; session 2: 342 ± 8 Ma) are in excellent agreement with expected values by ID-ICP-MCMS (1102 ± 5 Ma; Section 5.2.1) and LA-ICP-MS/MS (344 ± 2 Ma; Glorie et al., 2022), respectively (Table 2; Supplementary Data Fig. S1).

Sample 019-1315

Forty apatite targets were selected in sample 019-1315 for U-Pb geochronology. The majority of analyses (28/40) are dominated by the presence of Pb-inclusions that define multiple arrays in the Tera-Wasserburg plot. When only considering the relatively clean apatite signals, a U-Pb isochron lower intercept date of 1593 ± 69 Ma (MSWD: 0.93, N = 12) was obtained, with an initial $^{206}Pb/^{204}Pb$ ratio of 24.8 ± 8.1 and an initial $^{207}Pb/^{204}Pb$ ratio of 15.2 ± 2.4 (Fig. 5, Table 2). These initial Pb compositions are significantly different from the Stacey and Kramers (1975) ratios for early Mesoproterozoic apatite, and thus anchoring to Stacey and Kramers (1975) initial Pb was not preformed.

The apatite Lu-Hf inverse isochron date for this sample is 1576 ± 62 Ma (MSWD: 0.82, n = 29), with an initial $^{176}Hf/^{177}Hf$ of 0.282 ± 0.004. One analysis was removed due to poor signal quality.

Sample 019-1354

Thirty-eight apatite targets were selected in sample 019-1354 for U-Pb geochronology. Thirty-one of these analyses were dominated by Pb-bearing inclusions. Considering only the relatively

Table 1
Summary and petrological descriptions of analysed samples. Mineral abbreviations (in alphabetical order): anh: anhydrite, ap: apatite, ba: barite, bast: bastnäsite, chl: chlorite, cpy: chalcopyrite, dol: dolomite, hem: hematite, kspr: K-feldspar, mag: magnetite, moly: molybdenite, py: pyrite, qtz: quartz, ser: sericite, sid: siderite, sph: sphalerite.

Sample name	Sample description	minerals	Petrographic description	Dating methods
019-1263	Late dol vein with cpy	Dol, cpy	Late cross-cutting dol vein with large euhedral cpy and dol crystals forming in void.	Dol Lu-Hf
019-1315	Massive mag and pyr alteration. Evidence of Cu indicates cpy is present.	Mag, py, ap, sid, cpy, chl	The sample consists of massive Fe-oxide hydrothermal matrix with py, ap, cpy and sid +/- chl. Py occurs in matrix with cpy filling fractures. Ap occurs intergrown with both py and cpy, as well as separate grains within the matrix. The sample is magnetic, indicating that the Fe-oxide is mostly mag. Rare bladed Fe-oxides are present and form around blocky mag crystals.	Ap U-Pb, Ap Lu-Hf
019-1354	Banded hem (compositional layering.) assay data indicates elevated Pd	Hem, sid, chl. py, ap, cpy	This sample contains matrix of Fe-oxide-sid/chl around py crystals with cpy on edges/cracks. Py can be divided into two textures. The first py texture occurs as a ~1 cm nearly euhedral grain, surrounded by sid. This py grains show cpy forming along fractures and along grain edges. Ap, ch and hem form in association with the surrounding sid. The sid is in turn surrounded by a hem-sid-chl matrix. The second type of py occurs as ragged masses filled with many small ap inclusions, and hosted within hem-sid-chl-ap matrix. Cpy also occurs on its own as a ragged grain within the hem-sid-chl matrix. Fe-oxides show both bladed and blocky textures, possibly indicating original mag partly converted to hem.	Ap U-Pb, Ap Lu-Hf
019-1414	Fe-oxide with disseminated cpy	Hem, sid, cpy, Ap, qtz, dol, chl	The sample consists of ~100 – 200 μm circular features that have hem cores which are surrounded by sid, which are then rimmed by hem. They are further surrounded by cpy with minor ap, qtz, and chl. As both ap and cpy wrap the circular sid-hem features, they are interpreted to be cogenetic. The sample is devoid of py.	Ap Lu-Hf
019-1416	Carb-py vein cutting layered hydrothermal breccia	Dol, hem, cpy, chl, ap, sid	This sample consists of a dolomite-siderite vein with a large chalcopyrite grain. The vein cuts hematite-chlorite-siderite/dolomite with large chalcopyrite crystals as well as apatite and minor molybdenite (molybdenite appears part of the hematite-cpy-ap-chlor-siderite assemblage). Sample appears to contain no pyrite.	Moly Re-Os
019-1450	Dolomite vein with high Moly		This sample consists of hydrothermal dolomite vein in fairly typical hematite dominated hydrothermal matrix. Dolomite likely postdates matrix. The matrix consists of hematite-chlorite-pyrite-apatite with minor moly. The dolomite has a rim of quartz and Kspar that contains inclusions of chalcopyrite and barite.	Moly Re-Os
019-1552	carbonate vein cutting hydrothermal matrix/ breccia	Dol, cpy, hem, Ap, chl, py	This sample is a ~2 cm wide dol vein containing cpy. The vein cross cuts typical (of VUD019) 'steely' hem matrix (inferred to be hem-py-ap-sid.)	Dol Lu-Hf
019-1574	Similar to 019-1552	Dol, cpy	Sample contains dol veins (with cpy and reddish qtz) cutting/fracturing 'steely' hem breccia that contains py + cpy.	Dol Lu-Hf
019-1616	Carbonate vein cutting hydrothermal matrix/ breccia	Dol, Cpy, chl, moly	Sample consists of dolomite vein cutting Fe-oxide matrix. Hand sample vein is associated with chalcopyrite (but this is not evident in the polished rock block). Matrix consists of hem (non-magnetic), ap, chl, dol, moly. Ap and moly appear to form in similar areas of the matrix.	Moly Re-Os
019-1758	Sample contains extremely high LREEs. Breccia clasts surrounded by hydrothermal matrix.	Chl, bast, ser, qtz, cpy, hem, anh, moly, py	The sample consists of a breccia with extensively hydrothermally altered clasts. The matrix is fine-grained bladed bast, ser, and hem with euhedral moly flakes occurring in some sections. Clasts are generally heavily altered to chl with some ser and qtz. A few heavily fractured py grains occur. One sample shows a clast consisting of qtz with anh, cpy, and bladed hem forming in voids. This sample appears to contain no phosphates, and bast is the only carbonate mineral. Fe-oxide is hematite. Texturally, shows large bladed crystals and fractured blocky crystals	Bast Lu-Hf, Moly Re-Os
019-1846	Carbonate vein cross-cutting altered foliated rock	Dol, qtz, ser	This sample shows highly altered (ser?) and brecciated host rock with a cross-cutting large dol-qtz vein. No sign of mineralisation present.	Dol Lu-Hf
007-1143	Brecciated and altered rock with bladed hem	Hem, py, ap, chl, dol	Carbonate and py clasts in hem hydrothermal matrix. Breccia contains clasts of cpy. Matrix contains many ap grains, including a cluster of large grains.	Ap Lu-Hf
017-1210	Hydrothermal breccia.	Dol, sid, hem, py, qtz, Ap, chl, cpy	This sample shows the boundary between coarse breccia, and hydrothermal matrix similar to that observed in VUD019; hem-carb-chl (but with dol instead of sid). The hydrothermal breccia includes both clasts and crystals, and dolomite and siderite form euhedral to subhedral crystals. Based on the hand sample, the hem-dol-chl hydrothermal matrix fragment consists of a large (>2 cm) fragment within the breccia. Ap occurs throughout. Py occurs along the boundary between large hem-dol-chl fragment and coarse breccia. A single clast of cpy is surrounded by qtz was observed. Additionally, the block is cross-cut by a late (but very thin ~100 μm wide) dol + cpy vein. Fe-oxide in clast supported breccia is a mixture of early magnetite mostly replaced by haematite.	Dol and Sid Lu-Hf

Table 2
Summary of geochronological data obtained for the Vulcan prospect and for reference materials. Reference dates are from [1] Thompson et al. (2016), [2] Glorie et al. (2022) and [3] Tamblyn et al. (2024). The ID Lu-Hf data were obtained in this work (Fig. 4).

Sample	Mineral	Method	Age (Ma)	2SE (Ma)	MSWD	N
019-1315	apatite	U-Pb	1593	69	0.93	12
019-1315	apatite	Lu-Hf	1576	61	0.82	29
019-1354	apatite	U-Pb	1639	64	2.2	7
019-1354	apatite	Lu-Hf	1631	57	1.1	14
019-1414	apatite	Lu-Hf	1602	49	1.1	40
007-1143	apatite	Lu-Hf	1593	26	0.98	29
019-1263	dolomite	Lu-Hf (SES 1)	544	20	1.1	29
		Lu-Hf (SES 2)	544	25	0.6	14
019-1552	dolomite	Lu-Hf	553	16	1.0	23
019-1574	dolomite	Lu-Hf	589	48	0.51	19
019-1758	bastnäsite	Lu-Hf	1214	58	0.78	32
019-1846	dolomite	Lu-Hf	334.2	7.4	0.97	20
017-1210	dolomite	Lu-Hf	1572	36	1.2	21
017-1210	siderite	Lu-Hf	1485	76	1.4	15
019-1416	molybdenite	Re-Os	1609	22	0.87	5
019-1450	molybdenite	Re-Os	1596	23	0.43	4
019-1616	molybdenite	Re-Os	1572	11	1.4	24
019-1758	molybdenite	Re-Os	1586	9	1.4	55

Name	Mineral	Method	Session	Age (Ma)	2SE (Ma)	MSWD	N	Ref. age	2SE (Ma)	Ref. Method
401	apatite	U-Pb	20/01/22	526	4	1.7	28	525	8	LA U-Pb [1]
Bamble-1	apatite	Lu-Hf	24/01/22	1100	14	1.8	27	**1102**	**5**	***ID Lu-Hf***
			24/03/22	1104	14	0.65	23			
HR-1	apatite	Lu-Hf	24/01/22	344	4	0.46	27	344	2	LA Lu-Hf [2]
			24/03/22	342	8	0.32	12			
ME-1	calcite	Lu-Hf	13/04/22	1524	19	0.66	28	**1531**	**7**	***ID Lu-Hf***
			18/04/22	1535	19	0.97	23			
MDQ0252	moly.	Re-Os	04/03/22	1526	8	0.79	24	1520	3	*ID Re-Os*[3]
MDQ0221	moly.	Re-Os	04/03/22	1519	9	0.66	24	1523	6	*ID Re-Os*[3]

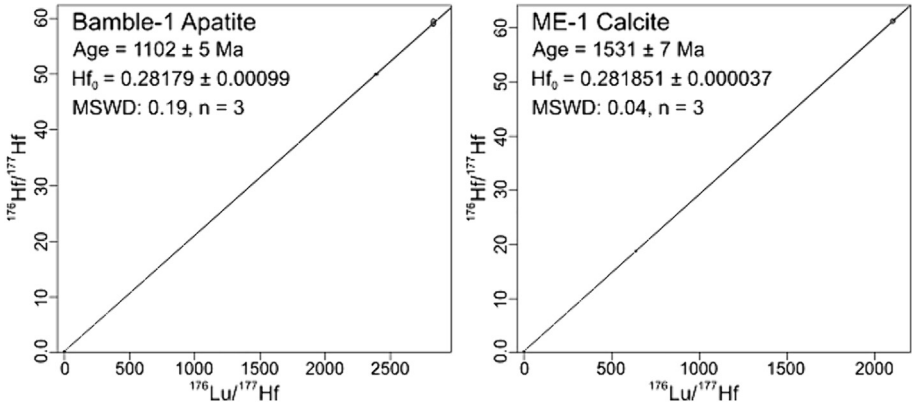

Fig. 4. Isotope-dilution Lu-Hf isochrons for the Bamble-1 apatite and ME-1 calcite reference materials, obtained by solution analyses using MC-ICPMS. Ellipses show 2σ uncertainties.

clean apatite signals, a U-Pb isochron lower intercept date of 1650 ± 109 Ma can be obtained (MSWD = 2.5, n = 7), with an ^{206}Pb/^{204}Pb ratio of 13.9 ± 15.0 and an initial ^{207}Pb/^{204}Pb ratio of 13.9 ± 5.0. When anchored to the Stacey and Kramers (1975) initial Pb composition, a U-Pb isochron lower intercept date of 1639 ± 64 Ma is produced (MSWD = 2.2, n = 7) (Fig. 5, Table 2).

The apatite Lu-Hf inverse isochron date for this sample is 1631 ± 57 Ma, with an initial ^{176}Hf/^{177}Hf of 0.279 ± 0.006 (MSWD: 1.1, n = 14). No analyses were excluded.

Sample 019-1414

Due to the dominance of Pb-bearing inclusions in all but one of the thirty-one time-resolved laser ablation signals for this sample, an apatite U-Pb date could not be obtained.

The inverse isochron Lu-Hf date of the apatite from this sample is 1602 ± 49 Ma, with an initial ^{176}Hf/^{177}Hf of 0.278 ± 0.008 (MSWD: 1.1, n = 40). No analyses were removed.

Sample 007-1143

The U-Pb data for sample 007-1143 is strongly contaminated by Pb inclusions and no U-Pb age could be calculated.

The Lu-Hf date for the apatite from this sample is 1593 ± 26 Ma, with an initial ^{176}Hf/^{177}Hf of 0.283 ± 0.040 (MSWD = 0.98, n = 29). One analysis was removed due to poor signal quality.

5.2.3. Carbonate Lu-Hf geochronology results for Vulcan

Carbonate U-Pb geochronology was not attempted given the very low U and high common-Pb concentrations in each sample. The LA-ICP-MS/MS calcite Lu-Hf data are presented as inverse isochrons, based on the ^{176}Lu/^{176}Hf and ^{177}Hf/^{176}Hf ratios, their 2σ uncertainties and uncertainty correlations. All carbonate dates have been calibrated for laser induced matrix-dependant fractionation against the MKED-1 calcite MCRM. The measured *in situ* Lu-Hf date for secondary reference material ME-1 (session 1:

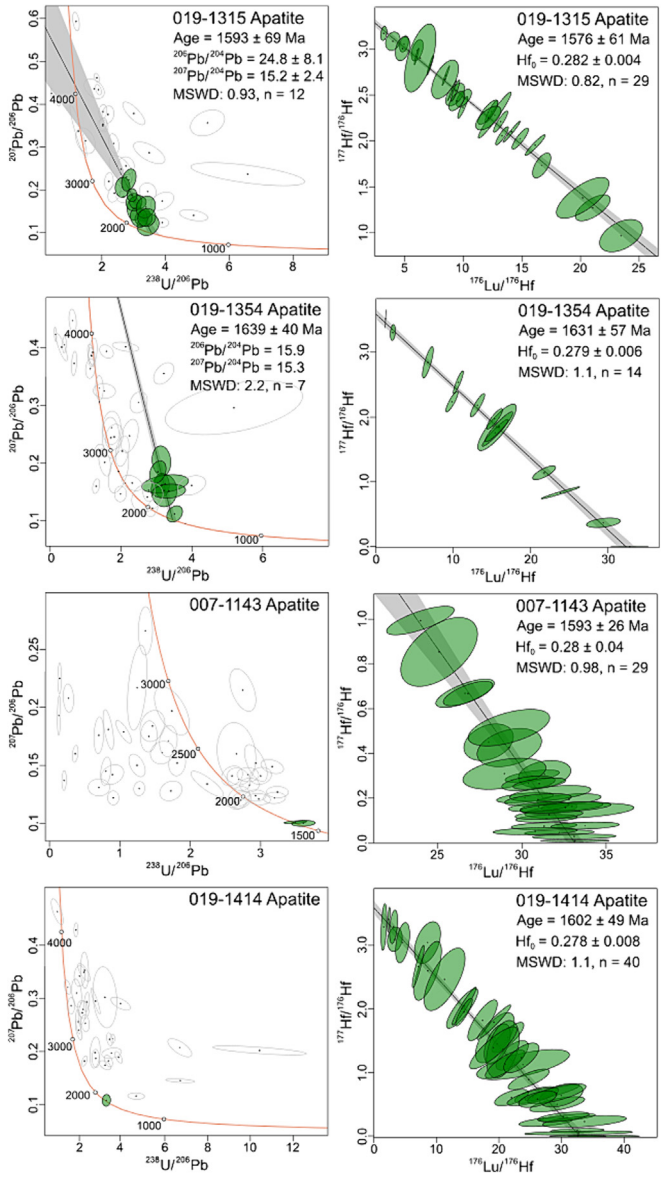

Fig. 5. Apatite U-Pb and Lu-Hf isochrons. U-Pb data is presented as Tera-Wasserberg concordia plots, and Lu-Hf data is presented as inverse isochron plots. Each row shows U-Pb data and Lu-Hf data from the same sample. Ellipses show 2σ uncertainties. Age uncertainties are 2SE. Pb_0 and Hf_0 refer to (respectively) the initial $^{207}Pb/^{206}Pb$ and $^{177}Hf/^{176}Hf$ ratios calculated from each isochron (Y-intercepts). Fe-Pb-rich inclusions were used to filter the U-Pb dataset (refer to Supplementary Data Figs. S3 and S4).

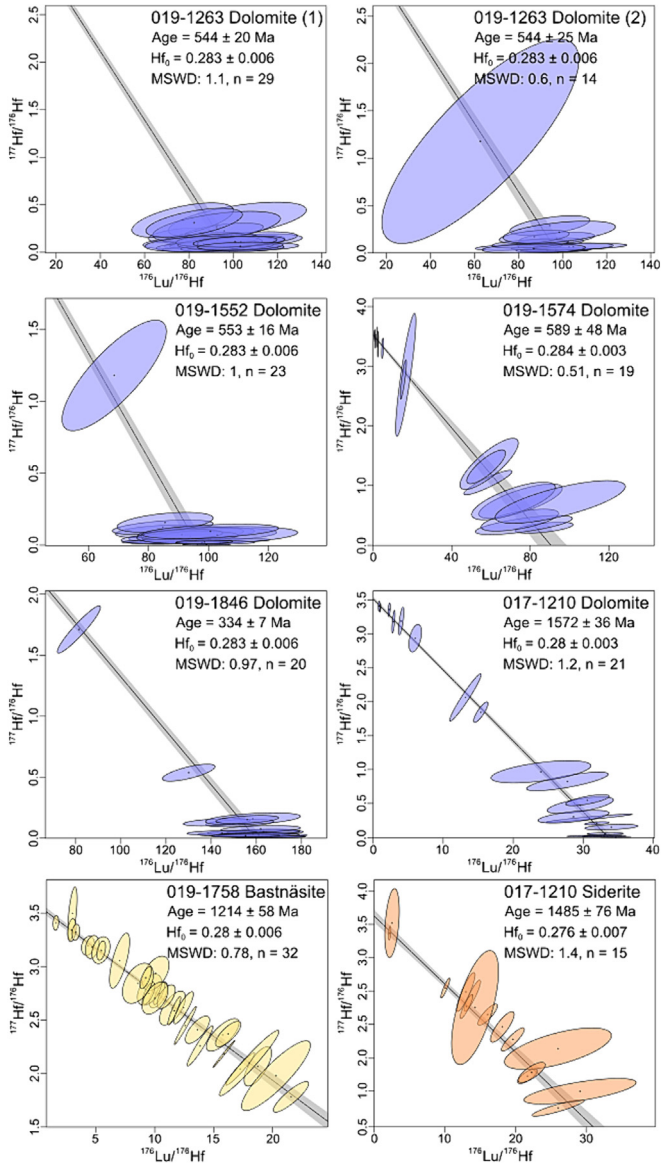

Fig. 6. Carbonate Lu-Hf inverse isochrons (blue = dolomite, orange = siderite, yellow = bastnäsite). The isochron regressions for samples 019–1263 and 019–1552 have been anchored to an initial $^{176}Hf/^{177}Hf$ of 0.2829 ± 0.003 (Vermeesch, 2024). Ellipses show 2σ uncertainties. Age uncertainties are 2SE. Pb_0 and Hf_0 refer to (respectively) the initial $^{207}Pb/^{206}Pb$ and $^{177}Hf/^{176}Hf$ ratios calculated from each isochron (as Y-intercepts). (For interpretation of the references to colour in this figure legend, the reader is referred to the web version of this article.)

1524 ± 19 Ma; session 2: 1535 ± 19 Ma) is in excellent agreement with the expected value from ID-ICP-MCMS (1531 ± 7 Ma; this work) (Table 2; Supplementary Data Fig. S1).

Sample 019-1263

The dolomite vein from sample 019-1263 yields highly radiogenic Hf compositions. Given these highly radiogenic $^{176}Hf/^{177}Hf$ compositions, the isochron was anchored to $^{176}Hf/^{177}Hf_i$ = 0.2829 ± 0.003 (Vermeesch, 2024), producing inverse Lu-Hf isochron dates of 544 ± 20 Ma (session 1, MSWD = 1.1, n = 29) and 544 ± 25 Ma (session 2, MSWD = 0.6, n = 14). One analysis was removed in each session due to poor signal quality.

Sample 019-1552

Similar to sample 019-1263, dolomite sample 019-1552 required an initial Hf anchor due to highly radiogenic Hf isotope compositions. The resultant anchored inverse isochron produced a Lu-Hf date of 553 ± 16 Ma (MSWD = 1.0, n = 23). Two analyses were removed due to poor signal quality.

Sample 019-1574

Dolomite sample 019-1574 contained inclusions with significantly higher $^{177}Hf/^{176}Hf$ ratios than observed in the previous samples. Consequently, rather than anchoring the dolomite Lu-Hf data to an assumed initial $^{177}Hf/^{176}Hf$ value, these inclusions were used in the isochron regression. A resultant date of 589 ± 48 Ma, with an initial $^{176}Hf/^{177}Hf$ ratio 0.283 ± 0.003 (MSWD = 0.51, n = 19) was produced. One analysis was removed in each session due to poor signal quality.

Sample 019-1846

Dolomite sample 019-1846 produced an anchored inverse isochron Lu-Hf date of 334.2 ± 7.4 Ma (MSWD = 0.97, n = 20). No data points were excluded.

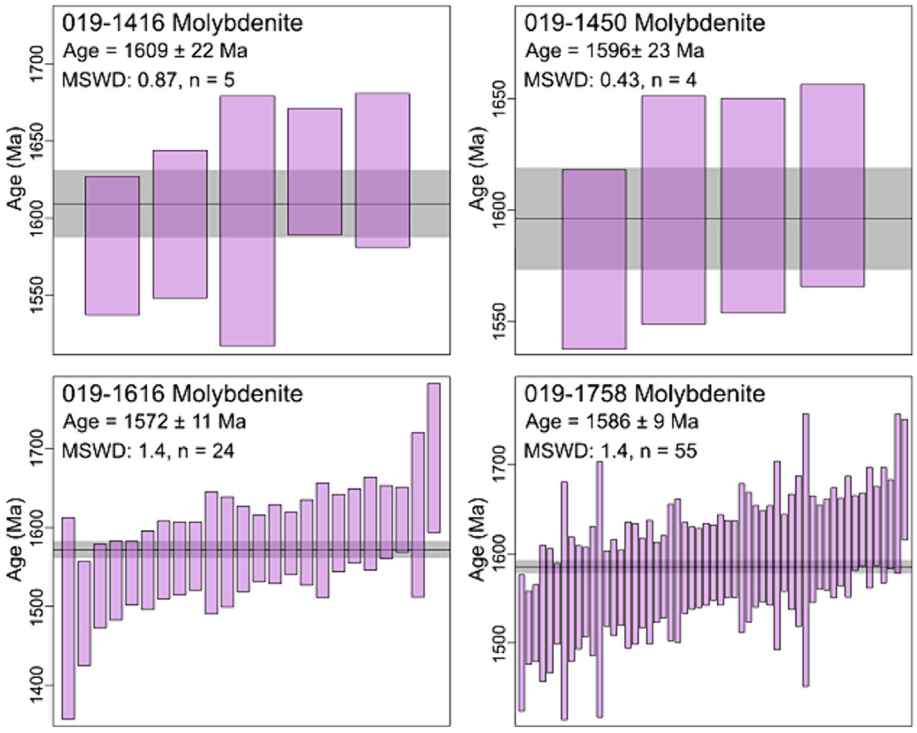

Fig. 7. Weighted mean molybdenite Re-Os dates and their 2SE uncertainties, calculated from the $^{187}Os/^{187}Re$ ratios and their 2σ uncertainties. There was no common Os detected in any analysis.

Sample 017-1210

Both siderite and dolomite were analysed from sample 017-1210. Similar to sample 019-1574, both the dolomite and siderite isochrons for this sample are anchored to inclusions.

The dolomite from this sample produced a Lu-Hf inverse isochron date of 1572 ± 36 Ma, with an initial $^{176}Hf/^{177}Hf$ ratio of 0.284 ± 0.003 (MSWD = 1.2, n = 21). One analysis was removed in each session due to poor signal quality.

Siderite from sample 017-1210 yields a Lu-Hf inverse isochron date of 1485 ± 76 Ma with an initial $^{176}Hf/^{177}Hf$ ratio of 0.277 ± 0.007 (MSWD = 1.4, n = 15). One outlier was removed due to poor time-resolved signal quality.

Sample 019-1758

Bastnäsite from sample 019-1758 produced a Lu-Hf inverse isochron date of 1214 ± 58 Ma with an initial $^{176}Hf/^{177}Hf$ ratio of 0.280 ± 0.003 (MSWD = 0.78, n = 32). No data was removed from the isochron.

5.2.4. LA-ICP-MS/MS Re-Os results for Vulcan

Given the absence of initial Os in the analysed samples, the Re-Os dates are presented as weighted means based on the $^{187}Os/^{187}Re$ ratios and their 2σ uncertainties. The measured *in situ* Re-Os dates for secondary reference materials MDQ0252 (1526 ± 8 Ma) and MDQ0221 (1519 ± 9 Ma) are in excellent agreement with reference values from ID-TIMS (1520 ± 3 Ma and 1523 ± 6 Ma, respectively; Tamblyn et al., 2024) (Table 2; Supplementary Data Fig. S2).

Samples 019-1416 and 019-1450

Two small molybdenite occurrences were sampled in close proximity (35 m) to each other. For both samples, only five and four Re-Os isotope analyses could be performed. The weighted mean Re-Os dates for both samples are consistent within uncertainty: 1609 ± 22 Ma (MSWD = 0.87) for sample 019-1416 and 1596 ± 23 Ma (MSWD = 0.43) for sample 019-1450.

Sample 019-1616

At total of twenty-six Re-Os isotope analyses were conducted for sample 019-1616, of which two were excluded due to poor signal quality and low Re concentrations. The resulting weighted mean Re-Os date is 1572 ± 11 Ma (MSWD = 1.4).

Sample 019-1758

For sample 019-1785, fifty-six Re-Os isotope analyses were conducted, of which one was removed due to poor signal quality (low Re). The resulting weighted mean Re-Os date is 1586 ± 9 Ma (MSWD = 1.4).

6. Discussion

6.1. Evaluating novel geochronometers for dating IOCG mineralisation

6.1.1. Apatite U-Pb vs. Lu-Hf

Apatite U-Pb data produced mostly highly scattered results in Tera-Wasserburg plots (Fig. 5), interpreted to be largely due to (i) significant contamination by Pb-bearing inclusions that are likely Fe-oxides and/or Fe-sulphides given high variability in the downhole Fe signals (Supplementary Data Fig. S3) and/or (ii) different degrees of U and/or Pb loss (e.g. Kirkland et al., 2018b). In more detail, non-contaminated U-Pb apatite signals tend to cluster or form linear arrays in Tera-Wasserburg plots (Fig. 5). A linear array on a Tera-Wasserburg indicates that data points reflect cogenetic apatite that crystallised with the same initial Pb composition (Tera and Wasserburg, 1972) as is expected for minerals with simple histories (i.e. no isotopic disturbances). Conversely, analyses with significant Fe contamination plot off the main isochron arrays (Supplementary Data Fig. S3). Consequently, we interpret the Fe-Pb-bearing inclusions to be a significant source of scatter on the isochron plots. This could be due to several reasons, including that the Pb inclusions are not cogenetic with the apatite, that the Pb

inclusions formed from a Pb reservoir that is significantly different to the apatite, or that the Pb inclusions have undergone post-formation Pb (and/or U) mobility. We note that these possibilities are not mutually exclusive.

Two out of four analysed apatite samples had sufficient inclusion-free analyses (12/40 for 019-1315 and 7/38 for 019-1354; Fig. 5, Supplementary Data Table S2), from which U-Pb isochron dates of 1593 ± 69 Ma and 1639 ± 64 Ma were calculated, respectively. The Lu-Hf dates for the same samples (1576 ± 61 Ma and 1631 ± 57 Ma, respectively) agree within uncertainty with the U-Pb dates and, although comparably imprecise, they can be regarded as more robust, given the entire dataset was used in the Lu-Hf isochron regressions. For the other two apatite samples (019-1414 and 007-1143), no meaningful U-Pb date could be obtained as all analyses are heavily contaminated by Pb-bearing inclusions and only produce scattered arrays in Tera-Wasserburg plots. For these samples, robust and internally consistent inverse isochron Lu-Hf dates of 1602 ± 49 Ma and 1593 ± 26 Ma, respectively, were produced, illustrating the power of the Lu-Hf method to derive meaningful isochron dates where the U-Pb method fails.

The apatite Lu-Hf analyses were applied to the same crystals and are contaminated by the same inclusions as the U-Pb data. However, these inclusions did not contain significant concentrations of either Lu or Hf, and consequently do not appear to have affected the Lu-Hf isotope ratios from which the Lu-Hf dates were calculated (Supplementary Data Fig. S3). This observation is consistent with the trace element data that suggests most of the inclusions are Fe-bearing phases such as Fe-oxides or Fe-sulphides, rather than Hf-enriched inclusions such as zircon. All Lu-Hf analyses for a given sample define a single isochron (pass the chi-squared test; MSWD ≤ expected for a single population; Spencer et al., 2016; Fig. 5), indicating negligible isotopic disturbance. We attribute this to the following reasons. Firstly, Hf is much less mobile compared to Pb in most fluids and mineral lattices (Brugger et al., 2016). Secondly, the $^{176}Hf/^{177}Hf$ ratio of the crustal reservoir is much less variable (crustal values range from ~0.280 to 0.283, with extreme values of ~0.286 documented; Salters and Zindler, 1995; Vervoort and Patchett, 1996; Iizuka et al., 2015; Fisher and Vervoort, 2018) relative to $^{207}Pb/^{206}Pb$ ratios, which have expected crustal values ranging from ~1.12 to ~0.835 (Stacey and Kramers, 1975) and can exceed this range significantly if the initial Pb is derived from the breakdown of a radiogenic Pb-rich reservoir (e.g. Romer and Wright, 1993; Kirkland et al., 2018a). The Lu-Hf isotopic system is also less prone to disturbance due to contamination from inclusions during laser ablation analysis than the U-Pb system because the most important Hf-bearing mineral in crustal rocks (zircon) has very low $^{176}Lu/^{177}Hf$ ratios (<0.001). Therefore, any contamination of apatite by zircon inclusions will only act to increase the $^{177}Hf/^{176}Hf$ ratio of the measurement (i.e., pushing the analyses toward the common-Hf, upper intercept of the isochron), without significantly affecting the resulting Lu-Hf dates (Fig. 6).

Hence, we demonstrate that the Lu-Hf system has several advantages over the U-Pb system as applied to dating IOCG systems. However, we acknowledge that although the apatite U-Pb dating undertaken in this study was of limited success, this may not be the case for all mineral deposits. Consequently, we suggest that double-dating of apatite using the Lu-Hf and U-Pb systems can produce the most reliable age constraints on apatite crystallisation and its associated mineralisation.

6.1.2. Carbonate Lu-Hf dating

Lutetium-Hf dating was conducted on dolomite crystals from two textural types: (i) blocky dolomite within a breccia (sample 017-1210) and (ii) late cross-cutting dolomite veins (samples 019-1263, 019-1552, 019-1574, 019-1846). Dolomite Lu-Hf analysis produced robust isochron dates, with the date for the breccia

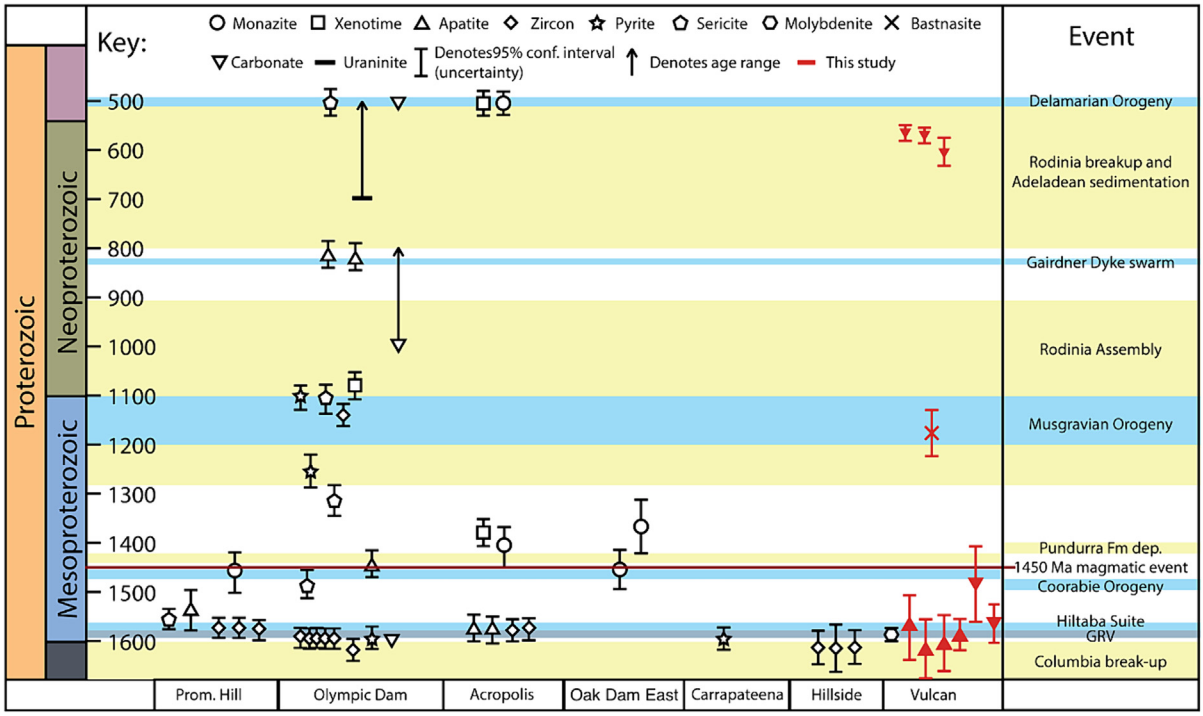

Fig. 8. Time space plot showing existing geochronology from IOCG mineral deposits and prospects in the Gawler Craton. Age ranges of major tectonic events are included (coloured bands). Red data points are from this study. Literature data: Prominent Hill: (Belperio et al., 2007; Bowden et al., 2017), Olympic dam: (Gustafson and Compston, 1979; McInnes et al., 2008; Maas et al., 2011, 2022; Jagodzinski, 2014; Huang et al., 2015; Apukhtina et al., 2017; Cherry et al., 2017, 2018; McPhie et al., 2020; Ehrig et al., 2021). Oak Dam: (Davidson et al., 2007). Carrapateena: (Sawyer, 2017). Acropolis: (Cherry et al., 2018; McPhie et al., 2020). Hillside: (Gregory et al., 2011). Vulcan: (Reid, 2019). (For interpretation of the references to colour in this figure legend, the reader is referred to the web version of this article.)

crystals (1572 ± 36 Ma) overlapping within uncertainty with the Lu-Hf dates obtained for apatite from the deposit (between ca. 1576 Ma and 1631 Ma; section 6.1.1). The late cross-cutting veins produced significantly younger Lu-Hf dates ranging between ca. 589 Ma and 334 Ma (Fig. 6). These are the first published laser ablation Lu-Hf dates for dolomite, demonstrating that dolomite Lu-Hf geochronology has the potential to be a useful tool for dating mineral deposits. However, in absence of age-constrained dolomite reference materials, the dolomite Lu-Hf dates are calibrated to the MKED-1 calcite reference material. Although the analyses of calcite and dolomite were conducted at the same analytical conditions (e.g. spot size, fluence, repetition rate), there is a possible matrix mismatch between the calibration material (calcite) and the analysed samples (dolomite). The effect of this different matrix on the Lu-Hf age is currently unknown, however, it is likely insignificant within the uncertainty of the resulting dates acquired in this study, given the good agreement between the apatite and dolomite Lu-Hf dates for the breccia samples. Consequently, the ca. 589–544 Ma and ca. 344 Ma dolomite Lu-Hf dates are considered accurate from an analytical standpoint.

An additional Lu-Hf date was obtained for siderite crystals that appear to be petrologically cogenetic with dolomite in sample 017-1210. This siderite Lu-Hf date of 1485 ± 76 Ma is within uncertainty of the dolomite Lu-Hf date of 1572 ± 36 Ma. However, while uncertainties overlap, the siderite is 87 million years younger when considering the absolute values only. The dolomite and siderite both occur as euhedral crystals within the breccia and provide a nucleation site for breccia matrix magnetite that was subsequently replaced by heamatite. Thus, both carbonates formed comparatively early in the paragenesis. This is consistent with the dolomite Lu-Hf date of 1572 ± 36 Ma. However, the difference between dolomite and siderite Lu-Hf dates might indicate, while the calcite reference material appears a valid calibration material for dolomite, it is less appropriate for siderite. However, it is important to emphasise that more data are needed to understand the accuracy of siderite Lu-Hf dating. More generally, successful application of both dolomite and siderite Lu-Hf requires elevated Lu concentrations and/or elevated Hf concentrations in order to produce good quality data, particularly in the case of siderite, which appears to incorporate less Lu than the dolomite in this study— an observation also made by Maas et al. (2022).

We also present the first published *in situ* bastnäsite Lu-Hf date (1214 ± 58 Ma; Fig. 6), calibrated to the MKED calcite reference material. Similar to siderite, it is important to emphasise that we currently lack a matrix-matched bastnaesite standard for laser ablation Lu-Hf analysis, and consequently the accuracy of this date can be questioned. The bastnäsite occurs as fine-grained crystals that form polycrystalline masses within veins and patches that are intergrown with molybdenite. The textural relationship with molybdenite suggests its primary growth age is ca. 1580 Ma. However, demonstrated matrix-related fractionation (before correction to a matrix-matched reference material) observed in crystalline minerals is generally between ca. 2% and 5% for laser ablation Lu-Hf (Simpson et al., 2021, 2022; Glorie et al., 2023, 2024b). Thus, while a better understanding of matrix fractionation in bastnäsite is required to fully constrain the true age, any additional correction is unlikely to shift the acquired age by more than 5%. We do however recognise that in some cases the analyses of bastnäsite represent ablation across at least several crystals, given the fine grain size. This multigrain sampling further complicates the interpretation of the bastnaesite Lu-Hf data. Nonetheless, we tentatively suggest the 1214 ± 58 Ma date records a period of hydrothermal activity and/or metamorphism that affected the Lu-Hf system in bastnäsite, but not the Re-Os system in molybdenite (below).

6.1.3. Molybdenite Re-Os dating

The new *in situ* molybdenite dates from Vulcan prospect range between ca. 1572 Ma and 1609 Ma (Fig. 7). Considering only samples with > 5 analyses, Re-Os dates are internally consistent with dates of 1572 ± 11 Ma and 1586 ± 9 Ma. These dates are in excellent agreement with a published conventional (isotope-dilution TIMS) Re-Os date of 1586 ± 8 Ma for the Vulcan prospect (Reid et al., 2013). Hence, the new *in situ* dates and associated calibration procedures are considered accurate, demonstrating the feasibility of the *in situ* Re-Os method to produce robust dates for molybdenite with a similar precision to conventional Re-Os geochronology.

6.2. Implications for the Vulcan IOCG system

The geochronological data from the Vulcan prospect produced in this study correspond to the timing of primary IOCG mineralisation across the Olympic Cu-Au Province. Hence, the applied methods can preserve accurate radiometric dates over a significant geological time period and have the potential to reconstruct prolonged and complex fluid-flow and thermal histories of ore deposits. The new dates produced in this study are summarised in Fig. 8 within the context of the geological history of the Olympic Cu-Au Province.

The majority of samples associated with brecciation and widespread hydrothermal alteration (including all dated apatite) produce dates of ca. 1.6 Ga. For instance, sample 019-1414, which has a clear relationship with Cu mineralisation (apatite and chalcopyrite both wrap around Fe-oxides; Fig. 3), produced an age of 1602 ± 49 Ma. Consequently, the primary stage of IOCG alteration and mineralisation at Vulcan is considered to be time-equivalent with regional constraints from Olympic Dam (ca. 1590 Ma) and previous Re-Os molybdenite geochronology from the prospect (1586 ± 8 Ma; Reid et al., 2013). Dolomite from drill core VUD017, approximately 4 km to the east of VUD019, (sample 017-1210), produced an age of 1572 ± 36 Ma (Fig. 6), which also overlaps with the interpreted primary mineralisation age for the prospect. This sample consists of largely euhedral dolomite crystals that likely formed early during hydrothermal brecciation, and suggest that brecciation at the deposit occurred soon after massive Fe-oxide formation. Consequently, the geochronological evidence suggests that widespread hydrothermal alteration occurred at the Vulcan prospect on a kilometre scale.

The bastnäsite date of 1214 ± 58 Ma is significantly younger than the apatite Lu-Hf dates. The closure temperature to volume diffusion of Lu and Hf is currently unknown for bastnäsite, and at least some of the bastnaesite Lu-Hf data was acquired from multigrain ablation. Consequently, it is unclear whether this date represents a resetting of the Lu-Hf system in bastnäsite or a primary crystallisation age. In the context of southern Australia, the Lu-Hf age derived from bastnäsite overlaps with the 1200–1160 Ma Musgravian Orogeny, a wide transcontinental, high-temperature orogenic event recorded in southern central Australia (Myers et al., 1996; Tucker et al., 2015; Walsh et al., 2015). The Musgravian Orogeny reworked the margins of the Gawler Craton (Hand et al., 2007), and broadly similar ages for REE mineralisation have been recorded at Olympic Dam (ca. 1.3 Ga; Maas et al., 2011). Preservation of such an age in bastnäsite in this study suggests that a regional Musgravian-aged hydrothermal event might have also affected the Vulcan prospect. Therefore, it is possible that there may be an episode of REE remobilisation at the Vulcan prospect that is not related to the original (ca. 1590 Ma) IOCG mineralisation. However, more data is needed to validate this interpretation.

The texturally late dolomite-chalcopyrite veins (Fig. 3) produced Lu-Hf dates of ca. 589–544 Ma (Fig. 6). These veins cross-

cut the ~1.6 Ga hematite-siderite-chlorite-apatite-sulphide hydrothermal matrix (Fig. 3), indicating vein formation post-dates the primary Cu mineralisation event. Given the clear occurrence of Cu in all analysed dolomite veins, we demonstrate that Cu was remobilised within the Vulcan prospect during the Ediacaran. Importantly, these veins are texturally different to the ca. 1574 Ma dolomite crystals, indicating there may be at least two stages of dolomite formation at Vulcan. Alternatively, the Ediacaran dolomite dates may reflect a resetting or 'closure' age for the Lu-Hf system in dolomite. However, there is currently insufficient understanding of trace element behaviour in dolomite to assess this possibility.

The age of Ediacaran dolomite veins in the Vulcan prospect broadly coincides with remobilisation of U and potentially Cu at Olympic Dam between ca. 0.7 Ga and 0.5 Ga (Fig. 8; Ehrig et al., 2021). Further evidence for Ediacaran regional fluid-flow in the Galwer Craton has been found from Cu remoblisation in ca. 0.5 Ga fluorite veins in the cover sequences of the Olympic Cu-Au Province (Glorie et al., 2023) and resetting of Rb-Sr systematics of shales in the Adelaide Rift Complex at 586 ± 30 Ma (Foden et al., 2001). Widespread clastic sedimentation also occurred across the Gawler Craton in response to overfilling of the Petermann Orogenic foreland in central Australia (Haines et al., 2001). The deposition of these sediments may have insulated the high-heat producing basement rocks of the Olympic Cu-Au province (McLaren et al., 2003), further promoting hydrothermal fluid flow (e.g. Oliver et al., 2006). Existing brecciation at the Vulcan prospect may have facilitated greater permeability relative to the surrounding and overlying rocks, allowing for concentrated fluid circulation and precipitation of veins. In summary, dolomite veining at Vulcan adds to the record of Ediacaran regional fluid-flow throughout the Gawler Craton, which was possibly driven by far-field tectonism. The presence of Cu-bearing minerals within the Ediacaran carbonate veins at Vulcan (Fig. 3) warrant further investigation into the extent to which this event has re-mobilised existing Cu mineralisation, introduced new Cu into the system, or transported Cu from basement-hosted ore systems, such as Vulcan, to form the sedimentary-hosted Cu deposits found in the Adelaidean strata overlying the Olympic Cu-Au Province (Selley, 2000).

Finally, for one sample a dolomite Lu-Hf date of 334 ± 7 Ma was obtained. This age corresponds with the Mount Eclipse Event (ca. 340–320 Ma; Bradshaw and Evans, 1988; Hand et al., 1999) of the intracratonic Alice Springs Orogeny. Considered the last event of the Alice Springs Orogeny, dominant expression of the Mount Eclipse Event has been constrained to amphibolite facies metamorphism and structural reworking in the Aileron Province of central Australia (Hand et al., 1999). Structural development and reactivation at that time has been observed in central and northern Australia, with southern extension into the Amadeus Basin (Bradshaw and Evans, 1988; Haines et al., 2001; Nixon et al., 2022a, Nixon et al., 2022b). While significant structural reactivation associated with this event has not previously been observed in southern Australia, typical deformation away from metamorphic reworking in northern Australia has presented as structural reactivation of weakened basement below cover (e.g. Warramunga Province; Nixon et al., 2022a). Analogous reactivation of weakened basement during this event provides a plausible mechanism for Carboniferous fluid flow in the Vulcan prospect.

7. Conclusions

We present *in situ* Lu-Hf dates for hydrothermal carbonates and apatite along with *in situ* dates for molybdenite using LA-ICP-MS/MS. Using two carbonate and apatite reference materials, the Lu-Hf protocol can be validated against isotope dilution MC-ICPMS dating. The data underscore the application of the new methodologies in ore deposit studies, allowing the following conclusions:

(i) We present the first *in situ* Lu-Hf dates for dolomite, siderite and bastnäsite, demonstrating the ability of the Lu-Hf system on a range of hydrothermal carbonates to date mineralisation processes.
(ii) In addition, we demonstrate that apatite Lu-Hf dating can provide more robust age constraints on mineralisation processes compared to the apatite U-Pb method.
(iii) Apatite and dolomite Lu-Hf dates as well as molybdenite Re-Os dates indicate widespread hydrothermal alteration and mineralisation in the Vulcan prospect occurred at ca. 1.6 Ga, consistent with previous constraints on IOCG mineralisation within the Gawler Craton (ca. 1595 Ma; e.g. Skirrow et al., 2007).
(iv) Further work is required to determine Lu-Hf closure temperatures, before dolomite, siderite and bastnäsite Lu-Hf ages can robustly be interpreted, however a dolomite date of 1574 ± 39 Ma overlaps with the ca. 1.6 Ga main mineralisation stage, suggesting that dolomite Lu-Hf isotopes can potentially preserve primary ages.
(v) New dolomite Lu-Hf dates provide further evidence for remobilisation of Cu throughout the Olympic Cu-Au Province during the Ediacaran, approximately 1 billion years after primary ore formation. The new geochronometers outlined in this study have the ability to provide robust temporal constraints on metal remobilisation, with potential implications for developing exploration models for secondary ore deposits in regional-scale mineral fields such as the Olympic Cu-Au Province.

CRediT authorship contribution statement

Alexander Simpson: Writing – original draft, Methodology, Investigation, Formal analysis, Conceptualization. **Stijn Glorie:** Writing – original draft, Writing – review & editing, Supervision, Methodology, Investigation, Funding acquisition, Conceptualization. **Martin Hand:** Writing – review & editing, Supervision, Investigation, Funding acquisition, Conceptualization. **Sarah E. Gilbert:** Writing – review & editing, Methodology, Formal analysis, Conceptualization. **Carl Spandler:** Writing – review & editing, Investigation, Funding acquisition, Conceptualization. **Marija Dmitrijeva:** Writing – review & editing, Resources. **Greg Swain:** Writing – review & editing, Resources, Funding acquisition. **Angus Nixon:** Writing – review & editing, Visualization, Investigation, Formal analysis. **Jacob Mulder:** Writing – review & editing, Visualization, Investigation. **Carsten Münker:** Writing – review & editing, Methodology, Investigation, Formal analysis.

Declaration of Competing Interest

The authors declare that they have no known competing financial interests or personal relationships that could have appeared to influence the work reported in this paper.

Acknowledgements

This paper was supported by an Accelerated Discovery Initiative Grant (ADI RD02/260), entitled 'Integrated Exploration Under Deep Cover' with joint funding from Fortescue and the Government of South Australia. SG was further supported by an Australian Research Council Future Fellowship (FT210100906). The acquisition of isotope-dilution Lu-Hf dates was financially supported by the Mineral Exploration Cooperative Research Centre whose activities are funded by the Australian Government's Cooperative

Research Centre Program. This is MinEx CRC Document 2024/11. CM thanks Frank Wombacher and Almut Katzemich for lab support. Chris Kirkland and an anonymous reviewer are thanked for their constructive reviews.

Appendix A. Supplementary data

Supplementary data to this article can be found online at https://doi.org/10.1016/j.gsf.2024.101867.

References

Apukhtina, O.B. et al., 2017. Early, deep magnetite-fluorapatite mineralization at the Olympic Dam Cu-U-Au-Ag deposit, South Australia. Econ. Geol. 112 (6), 1531–1542.

Babo, J. et al., 2017. The High-Grade Mo-Re Merlin Deposit, Cloncurry District, Australia: paragenesis and geochronology of hydrothermal alteration and ore formation. Econ. Geol. 112 (2), 397–422.

Barfod, G.H., Otero, O., Albarède, F., 2003. Phosphate Lu–Hf geochronology. Chem. Geol. 200 (3–4), 241–253.

Barfod, G.H., Krogstad, E.J., Frei, R., Albarède, F., 2005. Lu-Hf and PbSL geochronology of apatites from Proterozoic terranes: A first look at Lu-Hf isotopic closure in metamorphic apatite. Geochim. Cosmochim. Acta 69 (7), 1847–1859.

Bast, R. et al., 2015. A rapid and efficient ion-exchange chromatography for Lu–Hf, Sm–Nd, and Rb–Sr geochronology and the routine isotope analysis of sub-ng amounts of Hf by MC-ICP-MS. J. Anal. At. Spectrom 30 (11), 2323–2333.

Bastrakov, E.N., Skirrow, R.G., Davidson, G.J., 2007. Fluid Evolution and Origins of Iron Oxide Cu-Au Prospects in the Olympic Dam District, Gawler Craton. South Australia. Economic Geology 102 (8), 1415–1440.

Belperio, A., Flint, R., Freeman, H., 2007. Prominent Hill: A Hematite-Dominated, Iron Oxide Copper-Gold System. Econ. Geol. 102 (8), 1499–1510.

Bowden, B. et al., 2017. Age constraints on the hydrothermal history of the Prominent Hill iron oxide copper-gold deposit, South Australia. Mineralium Deposita 52 (6), 863–881.

Bradshaw, J.D., Evans, P.R., 1988. Palaeozoic Tectonics, Amadeus Basin, Central Australia. APPEA J. 28 (1), 267–282.

Brugger, J. et al., 2016. A review of the coordination chemistry of hydrothermal systems, or do coordination changes make ore deposits? Chem. Geol. 447, 219–253.

Campbell, L.S., Compston, W., Sircombe, K.N., Wilkinson, C.C., 2014. Zircon from the East Orebody of the Bayan Obo Fe–Nb–REE deposit, China, and SHRIMP ages for carbonatite-related magmatism and REE mineralization events. Contrib. Miner. Petrol. 168 (2), 1041.

Cave, B.W., Lilly, R., Glorie, S., Gillespie, J., 2018. Geology, Apatite Geochronology, and Geochemistry of the Ernest Henry Inter-lens: Implications for a Re-Examined Deposit Model. Minerals 8 (9), 405.

Cave, B., Lilly, R., Rea, P., 2022. In Situ U-Pb monazite geochronology records multiple events at the mount ISA Cu (± Zn-Pb-Ag) DEPOSIT, Northern Australia. Economic Geology 118 (1), 225–236.

Cherniak, D.J., Lanford, W.A., Ryerson, F.J., 1991. Lead diffusion in apatite and zircon using ion implantation and Rutherford backscattering techniques. Geochem. Geophys. Geosyst. 55, 1663–1673.

Cherry, A.R. et al., 2017. Linking Olympic Dam and the Cariewerloo Basin: Was a sedimentary basin involved in formation of the world's largest uranium deposit? Precambr. Res. 300, 168–180.

Cherry, A.R. et al., 2018. Tectonothermal events in the Olympic IOCG Province constrained by apatite and REE-phosphate geochronology. Aust. J. Earth Sci. 65 (5), 643–659.

Chew, D.M., Petrus, J.A., Kamber, B.S., 2014. U-Pb LA–ICPMS dating using accessory mineral standards with variable common Pb. Chem. Geol. 363, 185–199.

Ciobanu, C.L., Wade, B.P., Cook, N.J., Schmidt Mumm, A., Giles, D., 2013. Uranium-bearing hematite from the Olympic Dam Cu–U–Au deposit, South Australia: A geochemical tracer and reconnaissance Pb–Pb geochronometer. Precambr. Res. 238, 129–147.

Claoue-Long, J.C., King, R.W., Kerrich, R., 1990. Archaean hydrothermal zircon in the Abitibi greenstone belt: constraints on the timing of gold mineralisation. Earth Planet. Sci. Lett. 98 (1), 109–128.

Cochrane, R. et al., 2014. High temperature (>350°C) thermochronology and mechanisms of Pb loss in apatite. Geochim. Cosmochim. Acta 127, 39–56.

Corriveau, L., Montreuil, J.F., Potter, E.G., 2016. Alteration facies linkages among iron oxide copper-gold, iron oxide-apatite, and affiliated deposits in the great bear magmatic zone, Northwest Territories, Canada*. Econ. Geol. 111 (8), 2045–2072.

Courtney-Davies, L. et al., 2020. A Synthetic Haematite Reference Material for LA-ICP-MS U-Pb Geochronology and Application to Iron Oxide-Cu-Au Systems. Geostand. Geoanal. Res. 45 (1), 143–159.

Davidson, G.J., Paterson, H., Meffre, S., Berry, R.F., 2007. Characteristics and Origin of the Oak Dam East Breccia-Hosted, Iron Oxide Cu-U-(Au) Deposit: Olympic Dam Region, Gawler Craton, South Australia. Economic Geology 102 (8), 1471–1498.

Duncan, R.J. et al., 2011. A New Geochronological Framework for Mineralization and Alteration in the Selwyn-Mount Dore Corridor, Eastern Fold Belt, Mount Isa Inlier, Australia: Genetic Implications for Iron Oxide Copper-Gold Deposits. Econ. Geol. 106 (2), 169–192.

Duuring, P., Bleeker, W., Beresford, S.W., Hayward, N., 2010. Towards a volcanic–structural balance: relative importance of volcanism, folding, and remobilisation of nickel sulphides at the Perseverance Ni–Cu–(PGE) deposit. Western Australia. Mineralium Deposita 45 (3), 281–311.

Ehrig, K. et al., 2021. Staged formation of the supergiant Olympic Dam uranium deposit. Australia. Geology 49 (11), 1312–1316.

Faure, G., Mensing, T.M., 2005. Isotopes, principles and applications. John Wiley & Sons Inc, United States.

Fisher, C.M., Vervoort, J.D., 2018. Using the magmatic record to constrain the growth of continental crust—The Eoarchean zircon Hf record of Greenland. Earth Planet. Sci. Lett. 488, 79–91.

Foden, J., Barovich, K., Jane, M., O'Halloran, G., 2001. Sr-isotopic evidence for Late Neoproterozoic rifting in the Adelaide Geosyncline at 586 Ma: implications for a Cu ore forming fluid flux. Precambr. Res. 106 (3), 291–308.

Gilbert, S. et al., 2013. A Comparative Study of Five Reference Materials and the Lombard Meteorite for the Determination of the Platinum-Group Elements and Gold by LA-ICP-MS. Geostand. Geoanal. Res. 37 (1), 51–64.

Gilbert, S.E., Glorie, S., 2020. Removal of Hg interferences for common Pb correction when dating apatite and titanite by LA-ICP-MS/MS. J. Anal. At. Spectrom 35 (7), 1472–1481.

Gillespie, J. et al., 2022. Lu–Hf, Sm–Nd, and U-Pb isotopic coupling and decoupling in apatite. Geochim. Cosmochim. Acta 338, 121–135.

Glorie, S. et al., 2019b. Thermochronological and geochemical footprints of post-orogenic fluid alteration recorded in apatite: Implications for mineralisation in the Uzbek Tian Shan. Gondw. Res. 71, 1–15.

Glorie, S. et al., 2022. Detrital apatite Lu-Hf and U-Pb geochronology applied to the southwestern Siberian margin. Terra Nova 34 (3), 201–209.

Glorie, S. et al., 2023. Laser ablation (in situ) Lu-Hf dating of magmatic fluorite and hydrothermal fluorite-bearing veins. Geosci. Front. 14 (6), 101629.

Glorie, S. et al., 2024b. Robust laser ablation Lu–Hf dating of apatite: an empirical evaluation. Geol. Soc. Lond. Spec. Publ. 537 (1). SP537-2022-205.

Glorie, S., Hall, J.W., Nixon, A., Collins, A.S., Reid, A., 2019a. Carboniferous fault reactivation at the northern margin of the metal-rich Gawler Craton (South Australia): Implications for ore deposit exhumation and preservation. Ore Geol. Rev. 115, 103193.

Glorie, S., Gilbert, S.E., Hand, M., Lloyd, J.C., 2024a. Calibration methods for laser ablation Rb–Sr geochronology: comparisons and recommendation based on NIST glass and natural reference materials. Geochronology 6 (1), 21–36.

Gregory, C.J., Reid, A.J., Say, P., Teale, G.S., 2011. U-Pb geochronology of hydrothermal allanite and titanite and magmatic zircon from the Hillside Cu-Au deposit, Yorke Peninsula. South Australia. Department of Primary Industries and Resources. Report Book 2011/00003.

Haines, P.W., Hand, M., Sandiford, M., 2001. Palaeozoic synorogenic sedimentation in central and northern Australia: A review of distribution and timing with implications for the evolution of intracontinental orogens. Aust. J. Earth Sci. 48 (6), 911–928.

Hall, J.W. et al., 2018. Thermal history of the northern Olympic Domain, Gawler Craton; correlations between thermochronometric data and mineralising systems. Gondw. Res. 56, 90–104.

Hand, M., Mawby, J.O., Kinny, P., Foden, J., 1999. U-Pb ages from the Harts Range, central Australia: evidence for early Ordovician extension and constraints on Carboniferous metamorphism. J. Geol. Soc. London 156 (4), 715–730.

Hand, M., Reid, A., Jagodzinski, L., 2007. Tectonic Framework and Evolution of the Gawler Craton, Southern Australia. Econ. Geol. 102, 1377–1395.

Harlov, D.E., Wirth, R., Förster, H.-J., 2005. An experimental study of dissolution–reprecipitation in fluorapatite: fluid infiltration and the formation of monazite. Contrib. Miner. Petrol. 150 (3), 268–286.

Hogmalm, K.J., Dahlgren, I., Fridolfsson, I., Zack, T., 2019. First in situ Re-Os dating of molybdenite by LA-ICP-MS/MS. Miner. Deposita 54 (6), 821–828.

Hu, Z. et al., 2008. Signal enhancement in laser ablation ICP-MS by addition of nitrogen in the central channel gas. J. Anal. At. Spectrom 23 (8), 1093–1101.

Huang, Q. et al., 2015. Neoproterozoic (ca. 820–830 Ma) mafic dykes at Olympic Dam, South Australia: Links with the Gairdner Large Igneous Province. Precambr. Res. 271, 160–172.

Iizuka, T., Yamaguchi, T., Hibiya, Y., Amelin, Y., 2015. Meteorite zircon constraints on the bulk Lu-Hf isotope composition and early differentiation of the Earth. Proc. Natl. Acad. Sci. USA 112 (17), 5331–5336.

Gustafson, L., Compston, W., 1979. Rb-Sr dating of Olympic Dam core samples, Report to Western Mining Corporation, 18. Research School of Earth Sciences: Australian National University.

Jagodzinski, E., 2014. The age of magmatic and hydrothermal zircon at Olympic Dam. In: 2014 Australian Earth Sciences Convention (AESC), Sustainable Australia. Geological Society of Australia,Newcastle, New South Wales. July 7–10.

Johnson, J.P., Cross, K.C., 1995. U-Pb geochronological constraints on the genesis of the Olympic Dam Cu-U-Au-Ag deposit, South Australia. Econ. Geol. 90 (5), 1046–1063.

Kirkland, C.L. et al., 2018b. Apatite: a U-Pb thermochronometer or geochronometer? Lithos 318–319, 143–157.

Kirkland, C.L., Fougerouse, D., Reddy, S.M., Hollis, J., Saxey, D.W., 2018a. Assessing the mechanisms of common Pb incorporation into titanite. Chem. Geol. 483, 558–566.

Lagos, M. et al., 2007. High precision Lu–Hf geochronology of Eocene eclogite-facies rocks from Syros, Cyclades, Greece. Chem. Geol. 243 (1), 16–35.

Leach, D.L. et al., 2005. Sediment-Hosted Lead-Zinc Deposits: A Global Perspective. In: Hedenquist, J.W., Thompson, J.F.H., Goldfarb, R.J., Richards, J.P. (Eds.), One Hundredth Anniversary Volume. Society of Economic Geologists. https://doi.org/10.5382/AV100.18.
Maas, R. et al., 2011. Olympic Dam U-Cu-Au deposit, Australia: New age constraints. Mineral. Mag. 75, 1375.
Maas, R. et al., 2022. Carbonates at the supergiant Olympic Dam Cu-U-Au-Ag deposit, South Australia part 2: Sm-Nd, Lu-Hf and Sr-Pb isotope constraints on the chronology of carbonate deposition. Ore Geol. Rev. 140, 103745.
McCuaig, T.C., Beresford, S., Hronsky, J., 2010. Translating the mineral systems approach into an effective exploration targeting system. Ore Geol. Rev. 38 (3), 128–138.
McInnes, B.I.A., Keays, R.R., Lambert, D.D., Hellstrom, J., Allwood, J.S., 2008. Re–Os geochronology and isotope systematics of the Tanami, Tennant Creek and Olympic Dam Cu–Au deposits. Aust. J. Earth Sci. 55 (6–7), 967–981.
McLaren, S. et al., 2003. The hot southern continent: heat flow and heat production in Australian Proterozoic terranes. In: Hillis, R.R., Müller, R.D. (Eds.), Evolution and Dynamics of the Australian Plate. Geological Society of America. https://doi.org/10.1130/0-8137-2372-8.157.
McPhie, J., Kamenetsky, V.S., Chambefort, I., Ehrig, K., Green, N., 2011. Origin of the supergiant Olympic Dam Cu-U-Au-Ag deposit, South Australia: Was a sedimentary basin involved? Geology 39 (8), 795–798.
McPhie, J., Ehrig, K.J., Kamenetsky, M.B., Crowley, J.L., Kamenetsky, V.S., 2020. Geology of the Acropolis prospect, South Australia, constrained by high-precision CA-TIMS ages. Aust. J. Earth Sci. 67 (5), 699–716.
Münker, C., Weyer, S., Scherer, E., Mezger, K., 2001. Separation of high field strength elements (Nb, Ta, Zr, Hf) and Lu from rock samples for MC-ICPMS measurements. Geochem. Geophys. Geosyst. 2, 1064. https://doi.org/10.1029/2001GC000183.
Myers, J.S., Shaw, R.D., Tyler, I.M., 1996. Tectonic evolution of Proterozoic Australia. Tectonics 15 (6), 1431–1446.
Nixon, A.L. et al., 2022. Low-temperature thermal history of the McArthur Basin: Influence of the Cambrian Kalkarindji Large Igneous Province on hydrocarbon maturation. Basin Res. 34 (6), 1936–1959.
Nixon, A.L. et al., 2022a. Intracontinental Fault Reactivation in High Heat Production Areas of Central Australia: Insights From Apatite Fission Track Thermochronology. Geochemistry, Geophysics, Geosystems, 23(12): e2022GC010559.
Norris, A., Danyushevsky, L., 2018. Towards estimating the complete uncertainty budget of quantified results measured be LA-ICP-MS. Goldschmidt, Boston, USA.
Oliver, N.H.S. et al., 2006. 100th Anniversary Special Paper: Numerical Models of Extensional Deformation, Heat Transfer, and Fluid Flow across Basement-Cover Interfaces during Basin-Related Mineralization. Econ. Geol. 101 (1), 1–31.
Rasmussen, B., Fletcher, I.R., Muhling, J.R., Thorne, W.S., Broadbent, G.C., 2007. Prolonged history of episodic fluid flow in giant hematite ore bodies: Evidence from in situ U-Pb geochronology of hydrothermal xenotime. Earth Planet. Sci. Lett. 258 (1), 249–259.
Reeves, J.S., Cross, K.C., Oreskes, N., 1990. Olympic Dam copper-uranium-gold-silver deposit. Australasian Institute of Mining and Metallurgy 14, 1009–1135.
Reid, A., 2019. The Olympic Cu-Au Province, Gawler Craton: A Review of the Lithospheric Architecture, Geodynamic Setting, Alteration Systems, Cover Successions and Prospectivity. Minerals 9 (6), 371.
Reid, A., Smith, R.N., Baker, T., Jagodzinski, E.A., Selby, D., Gregory, C.J., Skirrow, R.G., 2013. Re-Os DATING OF Molybdenite within hematite breccias from the vulcan Cu-Au PROSPECT, Olympic Cu-Au Province, South Australia. Economic Geology 108 (4), 883–894. doi: https://doi.org/10.2113/econgeo.108.4.883
Roberts, N.M.W. et al., 2017. A calcite reference material for LA-ICP-MS U-Pb geochronology. Geochem. Geophys. Geosyst. 18 (7), 2807–2814.
Roberts, N.M.W. et al., 2020. Laser ablation inductively coupled plasma mass spectrometry (LA-ICP-MS) U-Pb carbonate geochronology: strategies, progress, and limitations. Geochronology 2 (1), 33–61.
Roberts, N.M.W., Walker, R.J., 2016. U-Pb geochronology of calcite-mineralized faults: Absolute timing of rift-related fault events on the northeast Atlantic margin. Geology 44 (7), 531–534.
Romer, R.L., Wright, J.E., 1993. Lead mobilization during tectonic reactivation of the western Baltic Shield. Geochim. Cosmochim. Acta 57 (11), 2555–2570.
Salters, V.J.M., Zindler, A., 1995. Extreme 176Hf/177Hf in the sub-oceanic mantle. Earth Planet. Sci. Lett. 129 (1), 13–30.
Sawyer, M., 2017. Carrapateena iron oxide Cu-Au-Ag-U deposit. In: Phillips, G.N. (Ed.), Australian Ore Deposits. The Australasian Institute of Mining and Metallurgy, Australia, pp. 615–620.
Scherer, E., Münker, C., Mezger, K., 2001. Calibration of the Lutetium-Hafnium Clock. Science 293 (5530), 683–687.
Selby, D., Creaser, R.A., 2001. Re-Os Geochronology and Systematics in Molybdenite from the Endako Porphyry Molybdenum Deposit, British Columbia. Canada. Economic Geology 96 (1), 197–204.
Selley, D., 2000. Geological framework and copper mineralsation in South Australia, AMIRA Project P544 - Proterozoic sediment-hosted copper deposits. Pongratz and Blake Production.
Simpson, A. et al., 2021. In-situ LuHf geochronology of garnet, apatite and xenotime by LA ICP MS/MS. Chem. Geol. 577, 120299.
Simpson, A. et al., 2022. In situ Lu–Hf geochronology of calcite. Geochronology 4 (1), 353–372.
Skirrow, R. et al., 2007. Timing of Iron Oxide Cu-Au-(U) hydrothermal activity and Nd isotope constraints on metal sources in the Gawler Craton, South Australia. Econ. Geol. 102, 1441–1470.
Skirrow, R.G., 2022. Iron oxide copper-gold (IOCG) deposits – A review (part 1): Settings, mineralogy, ore geochemistry and classification. Ore Geol. Rev. 140, 104569.
Skirrow, R., Maas, R., Ashley, P.M., 1999. New age constraints for Cu-Au(-Mo) mineralisation and regional alteration in the Olary-Broken hill region. AGSO Research Newsletter 31.
Söderlund, U., Patchett, P.J., Vervoort, J.D., Isachsen, C.E., 2004. The 176Lu decay constant determined by Lu–Hf and U-Pb isotope systematics of Precambrian mafic intrusions. Earth Planet. Sci. Lett. 219 (3), 311–324.
Spandler, C. et al., 2016. MKED1: A new titanite standard for in situ analysis of Sm–Nd isotopes and U-Pb geochronology. Chem. Geol. 425, 110–126.
Spencer, C.J., Kirkland, C.L., Taylor, R.J.M., 2016. Strategies towards statistically robust interpretations of in situ U-Pb zircon geochronology. Geosci. Front. 7 (4), 581–589.
Sprung, P., Scherer, E.E., Upadhyay, D., Leya, I., Mezger, K., 2010. Non-nucleosynthetic heterogeneity in non-radiogenic stable Hf isotopes: Implications for early solar system chronology. Earth Planet. Sci. Lett. 295 (1), 1–11.
Stacey, J.S., Kramers, J.D., 1975. Approximation of terrestrial lead isotope evolution by a two-stage model. Earth Planet. Sci. Lett. 26 (2), 207–221.
Tera, F., Wasserburg, G.J., 1972. U-Th-Pb systematics in three Apollo 14 basalts and the problem of initial Pb in lunar rocks. Earth and Planetary Science Letters 14, 36–51.
Thompson, J. et al., 2016. Matrix effects in Pb/U measurements during LA-ICP-MS analysis of the mineral apatite. J. Anal. At. Spectrom 31 (6), 1206–1215.
Thomson, S.N., Gehrels, G.E., Ruiz, J., Buchwaldt, R., 2012. Routine low-damage apatite U-Pb dating using laser ablation-multicollector-ICPMS. Geochem. Geophys. Geosyst. 13 (2), Q0AA21.
Tucker, N.M., Hand, M., Kelsey, D.E., Dutch, R.A., 2015. A duality of timescales: Short-lived ultrahigh temperature metamorphism preserving a long-lived monazite growth history in the Grenvillian Musgrave–Albany–Fraser Orogen. Precambr. Res. 264, 204–234.
Vermeesch, P., 2018. IsoplotR: A free and open toolbox for geochronology. Geosci. Front. 9 (5), 1479–1493.
Vermeesch, P., 2024. (anchored) isochrons in IsoplotR. Geochronology Discuss. 2024, 1–16.
Vervoort, J., Patchett, P.J., 1996. Behavior of hafnium and neodymium isotopes in the crust: constraints from Precambrian crustally derived granites. Geochim. Cosmochim. Acta 60 (19), 3717–3733.
Walsh, A.K. et al., 2015. P-T–t evolution of a large, long-lived, ultrahigh-temperature Grenvillian belt in central Australia. Gondw. Res. 28 (2), 531–564.
Wilke, M. et al., 2012. Zircon solubility and zirconium complexation in H2O+Na2O +SiO2±Al2O3 fluids at high pressure and temperature. Earth Planet. Sci. Lett. 349–350, 15–25.
Zhai, W. et al., 2022. Hydrothermal zircon: Characteristics, genesis and metallogenic implications. Ore Geol. Rev. 149, 105111.
Tamblyn, R., Gilbert, S., Glorie, S., Spandler, C., Simpson, A., Hand, M., Hasterok, D., Ware, B. Tessalina, S., 2024. Molybdenite Reference Materials for In Situ LA-ICP-MS/MS Re-Os Geochronology. Geostand Geoanal Res. (in press). https://doi.org/10.1111/ggr.12550.